

1 **UNCERTAINTY ESTIMATION OF REGIONALISED DEPTH-DURATION-FREQUENCY CURVES IN**
2 **GERMANY**

3 *Bora Shehu^{1,2}, Uwe Haberlandt¹*

4 ¹ Institute of Hydrology and Water Resources Management, Leibniz University of Hannover, Hannover, Germany

5 ² Institute of Environmental Sciences and Geography, University of Potsdam, Potsdam, Germany

6 *Correspondence to: Bora Shehu (bora.shehu@uni-potsdam.de)*

7 **ABSTRACT:**

8 The estimation of rainfall depth-duration-frequency (DDF) curves is necessary for the design of several water systems
9 and protection works. These curves are typically estimated from observed locations, but due to different sources of
10 uncertainties, the risk may be underestimated. Therefore, it becomes crucial to quantify the uncertainty ranges of such
11 curves. For this purpose, the propagation of different uncertainty sources in the regionalisation of the DDF curves for
12 Germany is investigated. Annual extremes are extracted at each location for different durations (from 5mins up to 7days),
13 and local extreme value analysis is performed according to Koutsoyiannis et al. (1998). Following this analysis, five
14 parameters are obtained for each station, from which four are interpolated using external drift kriging, while one is kept
15 constant over the whole region. Finally, quantiles are derived for each location, duration and given return period. Through
16 a non-parametric bootstrap and geostatistical spatial simulations, the uncertainty is estimated in terms of precision (width
17 of 95% confidence interval) and accuracy (expected error) for three different components of the regionalisation: i) local
18 estimation of parameters, ii) variogram estimation and iii) spatial estimation of parameters. First two methods were tested
19 for their suitability in generating multiple equiprobable spatial simulations: sequential Gaussian simulations (SGS) and
20 simulated annealing (SA) simulations. Between the two, SGS proved to be more accurate and was chosen for the
21 uncertainty estimation from spatial simulations. Next, 100 realisations were run at each component of the regionalisation
22 procedure to investigate their impact on the final regionalisation of parameters and DDFs curves, and later combined
23 simulations were performed to propagate the uncertainty from the main components to the final DDFs curves. It was
24 found that spatial estimation is the major uncertainty component in the chosen regionalisation procedure, followed by the
25 local estimation of rainfall extremes. In particular, the variogram uncertainty had very little effect in the overall estimation
26 of DDFs curves. We conclude that the best way to estimate the total uncertainty consisted of a combination between local
27 resampling and spatial simulations, which resulted in more precise estimation at long observation locations, and a decline
28 in precision at un-observed locations according to the distance and density of the observations in the vicinity. Through
29 this combination, the total uncertainty was simulated by 10,000 runs in Germany, and indicated, that depending on the
30 location and duration level, tolerance ranges from ±10-30% for low return periods (lower than 10 years), and from ±15-
31 60% for high return periods (higher than 10 years) should be expected, with the very short durations (5min) being more
32 uncertain than long durations.

33 **KEYWORDS:**

34 Depth-Duration-Frequency Curves, external drift kriging, local uncertainty, variogram uncertainty, spatial uncertainty,
35 sequential Gaussian simulation

1. Introduction

Design precipitation volumes at different duration and frequencies, also known as Depth-Duration-Frequency (DDF) Curves, are necessary for the design of many water-related systems and facilities. These curves are typically generated by fitting a theoretical distribution to the rainfall extremes (either annual extremes – AMS or extremes above a threshold – POT) derived for specific duration intervals at observed locations. Mostly, a Generalised Extreme Value distribution with three parameters (location, scale and shape) is preferred for such applications (Koutsoyiannis, 2004a, 2004b). An adjustment of the rainfall extremes over different duration intervals is also considered either before fitting the theoretical distribution (as in Koutsoyiannis et al. 1998), or after (as in Fischer and Schumann, 2018). As the fitted theoretical distribution can be used to describe the DDF values only at observed locations, regionalisation techniques are applied to estimate these distributions at unobserved locations. The estimation of a regional distribution based on the index method as proposed by Hosking and Wallis (1997) is one of the most used methods in the literature (Burn, 2014; Forestieri et al., 2018; Perica et al., 2019), followed by the kriging interpolation of the parameters describing these theoretical distributions (Ceresetti et al., 2012; Shehu et al., 2022; Uboldi et al., 2014).

Nevertheless, the procedure for the derivation of DDF curves is subjected to different sources of uncertainty which can affect the confidence level of the estimated design values. Such sources of uncertainties include measurement errors, choice of distribution, short observation length, non-representativeness of point measurements for the spatial dependency of extremes, in-stationarity due to the climate change etc (Marra et al., 2019b). So far for DDF curves in Germany, there is not objective quantification of the uncertainty, but only approximative guessed tolerance ranges between 10-20% (depending on the return period) that should account for the measurement errors, uncertainties in the extreme value estimation and regionalisation, and for the climate variability (Junghänel et al., 2017). The tolerance ranges are kept constant throughout duration levels and locations, nevertheless such tolerance ranges are expected to be higher for very short observations and high return periods (Poschlod, 2021) especially for short durations and drier climate (Marra et al., 2017). Therefore, there is a need to perform different simulations in order to quantify the tolerance ranges (uncertainty) dependent on duration, location and return period. In this paper, the focus is on developing a framework that accounts for uncertainties due to short observation lengths and non-representativeness of point measurements for spatial dependencies of extremes. Once a framework is developed, it can be used to investigate the role of distribution choice as in Miniussi and Marra (2021) or the role of future climate as in Poschlod (2021).

In the literature, parametric or non-parametric bootstrapping resampling techniques are used to quantify tolerance ranges of DDF curves. Overeem et al., (2008) was one of the first to include the uncertainty of such curves by including only the uncertainty of GEV parameters estimated by a regional bootstrap procedure (sample variability). In their study, extremes from a homogenous region were pooled together to estimate regional probability distribution, which resulted in a narrower uncertainty range at observed locations. Overeem et al. (2009) proposed a bootstrapping technique where same years for all the observed points were resampled together in order to maintain the spatial dependency of the extremes. Uboldi et al. (2014) went a step further and accounted spatial dependency when performing the bootstrapping for each location: extremes from near observations have a higher probability to be resampled at a specific location than the ones from far away. Typically, the bootstrapping procedures are implemented together with the index-based regionalisation as proposed by Hosking and Wallis (1997). Examples in the literature of such applications, are for instance in Burn (2014) and Requena et al. (2019) in Canada where the uncertainty is computed from the confidence intervals of a parametric bootstrap procedure, or in Chaudhuri and Sharma (2020), Notaro et al. (2015), Tfwala et al. (2017), Van de Vyver (2015) where a Bayesian framework is employed to estimate the uncertainty of DDFs curves at different duration levels. Mostly the uncertainty is derived from bootstrap procedure where the 95% or 90% confidence interval width is used as a measure of precision: as lower the confidence interval width, the more precise are the estimates. However, the spatial structure of

78 uncertainties is not well considered in the index-based regionalisation: first, no uncertainty of the index itself is considered
79 and propagated, and second, there is no measure how uncertain the locations further away from observations are.
80 Therefore, local resampling of extreme values (to account for sample variability) are not enough to describe the spatial
81 structure of uncertainty, instead spatial simulations are needed. Alternatively, remote sensing data, i.e. satellites or weather
82 radar data, provide spatially continuous indirect measurements of rainfall intensities or volumes (Marra et al., 2019b).
83 However, their shortcomings are related to the short available dataset, the inability of the remote sensing dataset to capture
84 accurately intensities, and lack of a true observed dataset to validate the methods applied. While remote sensing provides
85 a valuable tool and more research is performed in tackling better the uncertainties, at the moment DDF curves from station
86 observations represent still the standard procedure, and hence a method to estimate the spatial structure of uncertainties
87 based on these observations is required.

88 In kriging, when regionalising from point values, the variance of the estimations can be used as a measure of the
89 uncertainty for un-observed locations. This estimation can either be parametric (multi-Gaussian process) or non-
90 parametric (indicator kriging). It is widely accepted that the kriging system can capture only the local uncertainty
91 (providing information at one location at a time conditioned to other observations in the vicinity) and not the spatial one
92 (providing a measure of uncertainty about the un-sampled values taken altogether in space rather than one by one), the
93 estimated uncertainty is dependable on the data configuration rather than on the value itself, and lastly it fails to preserve
94 the high spatial variability of the target variable (Cinnirella et al., 2005; Deutsch and Journel, 1998; Goovaerts, 1999b,
95 2001; Lin and Chang, 2000). As stated in Liao et al. (2016) the spatial uncertainty is more important (bigger) than the
96 local uncertainty. Therefore, solutions for the estimation of the spatial uncertainties in geostatistics are stochastic
97 simulations with equiprobable realisation of the target variable in space. The main assumption of the stochastic
98 simulations is the generation of equiprobable realisations in space while maintaining certain global statistics of the target
99 variable; for instance, the histogram of the observed values and the semi-variogram (herein referred as variogram for
100 simplicity) - which describes the spatial dependency of the variable variance on the distance between the observations.
101 The stochastic simulations present a trade-off: on one side they provide more spatial variable fields than kriging (which
102 is known for its smoothing properties), and on the other side, because the goal is to maintain the global statistics, may
103 suffer from larger errors at the local scale. Another advantage of stochastic simulations is the ability to compute directly
104 the confidence intervals for the target variable, while in kriging interpolation the confidence intervals are computed from
105 the kriging variance assuming a normal distribution of the errors.

106 Examples of different stochastic simulations are the sequential Gaussian simulations (SGS) (Cinnirella et al., 2005; Emery,
107 2010; Ersoy and Yünsel, 2009; Gyasi-Agyei and Pegram, 2014; Jang, 2015; Jang and Huang, 2017; Liao et al., 2016;
108 Poggio et al., 2010; Ribeiro and Pereira, 2018; Szatmári and Pásztor, 2019; Varouchakis, 2021; Yang et al., 2018),
109 sequential indicator simulations (SIS) (Bastante et al., 2008; Goovaerts, 1999a, 2001; Luca et al., 2007), simulated
110 annealing (SA) (Goovaerts, 2000; Hofmann et al., 2010; Lin and Chang, 2000), turning bands (TB) (Namysłowska-
111 Wilczyńska, 2015) etc. As seen, the most preferred stochastic simulation in the literature is the SGS due to its simplicity,
112 followed by the SIS and then by SA. Alternatively a stochastic random mixing (as stated in Bárdossy and Hörning, 2016)
113 with spatial dependency modelled by Copulas (Haese et al., 2017) or a collocated cokriging simulation (Bourennane et
114 al., 2007) can also be applied. However, geostatistical simulations remain the preferred choice in the literature for
115 estimating spatial uncertainty, although the main application is in the geosciences field, with very few applications in
116 rainfall modelling, and to authors knowledge no application to the regionalisation of extreme design rainfall. Therefore,
117 geostatistics becomes a useful tool to estimate and analyse the estimation of DDF uncertainties at observed and un-
118 observed locations. The question which of stochastic simulations is more appropriate for extreme design rainfall naturally
119 raises.

120 As stated, because of its simplicity the SGS is a very popular method in estimating spatial uncertainty in geostatistics. In
121 the SGS approach each simulation is considered a realisation of the multivariate Gaussian process, and hence it is strictly
122 required for the target variable to be multivariate normal. As discussed in Deutsch and Journel (1998), the testing of the
123 multivariate normality is a difficult task, which depending on the case at hand, can be very time and computational
124 expensive and hence is not usually tested. Typically, studies in literature include a transformation to normal distribution
125 in order to ensure that the target variable is at least univariate normal. Another disadvantage of the normalisation needed
126 for the SGS application, is that the upper and lower tail of the transformed variable will cause an under/over – estimation
127 of these values, and hence an extrapolation to lower and upper bounds is required. Contrary, to the SGS, the sequential
128 indicator simulations (SIS) does not need a prior assumption on the multivariate normality of the target variable and is
129 more suitable for observed values that do not exhibit bivariate normal properties. The SIS is a conditional simulation
130 based on the indicator kriging theory, which provides the probability that a location has to exceed a certain threshold. The
131 number of thresholds considered should be more than 5 but lower than 15 as suggested by Luca et al. (2007). For each of
132 the selected threshold a variogram is fitted to the portion of the data following under this threshold, and it is used for the
133 sequential simulation. A disadvantage of the SIS is that, if many threshold classes are presented, order relationship
134 problems will arise on the obtained realisations (Deutsch and Journel, 1998; Journel and Posa, 1990), which are more
135 emphasized if empty thresholds are included (Luca et al., 2007). Another disadvantage of the SIS is that mainly it has
136 been used together with simple and ordinary kriging theory (Deutsch and Journel, 1998), and no application of the SIS in
137 an external drift or universal kriging has been reported (to authors knowledge) in the literature. Alternative to the SGS
138 and SIS stochastic simulations, the simulated annealing (SA) can be also implemented to alternate and generate
139 conditional images of a continuous target variable. The main idea in the implementation of the SA, is a numerical
140 algorithm which perturbs continuously an image until an objective criterion is reached. The optimization function can
141 include only one criterion (typically the global statistics) or multiple criteria depending on the application at hand. For
142 instance Goovaerts (2000) included three criteria: the local estimation of the variable, the observed histogram and
143 variogram. The advantage of the SA is that no prior assumption of the normality is required (as the observed histogram is
144 reproduced) and that it allows a degree of flexibility for realisations that doesn't exactly match the objective criteria. On
145 the other hand, the disadvantages of the SA include the prior selection of the objective criteria carefully and, depending
146 on the application, the high computational time.

147 In our previous study, Shehu et al. (2022) investigated different methods and datasets in Germany for the local estimation
148 of the DDFs from station data, and different regionalisation methods for the estimation of the DDFs at ungauged locations.
149 The study revealed that kriging interpolation of long observation records (more than 40 years) with a denser network of
150 short observations as an external drift delivered best cross-validation results for return periods higher than 10 years.
151 Therefore, apart from the stochastic simulations that account for the spatial uncertainty, more simulations are needed to
152 tackle other sources of uncertainties for the estimation of DDF curves: such as sample variability, variogram estimation
153 and the combination with an external drift. For this purpose, the SGS and SA will be implemented and investigated for
154 their suitability in generating spatial simulations for DDF curves. Once a best method is chosen for this purpose, different
155 experiments are conducted based on non-parametric bootstrapping techniques to investigate how each of the uncertainty
156 component is propagated into the final DDF curves, and if some components are more dominant than others. Lastly, based
157 on the most important components, a framework for estimating the total uncertainty in regionalised DDF curves (both at
158 observed and un-observed locations) is proposed.

159 The paper is organized as following: First, in Section 2 the data and methods for the estimation and regionalisation of
160 DDF curves is explained (Section 2.1 and 2.2), together with the necessary transformation to normality in Section 2.3 and
161 testing the bi-Gaussian conditions in Section 2.4. Then an introduction to the main uncertainty sources considered here is

162 given in Section 3, and the main methods to tackle each uncertainty sources are given in Section 3.1 to 3.3. An overview
163 of the experiments and how the uncertainty is measured in terms of both accuracy and precision is described in Section
164 3.4. The results are summarised in section 4, where first a comparison of the two spatial simulations techniques is
165 investigated (Section 4.1), and later uncertainty results of different experiments for un-observations locations and for the
166 whole German region are shown respectively in Section 4.2 and Section 4.3. Lastly conclusions and the best framework
167 to tackle uncertainties for DDF curves in Germany are discussed in Section 5.

168 2. Study Area and Data Processing

169 The investigation is carried out for Germany, as shown in **Figure 1**, together with the two rainfall measuring networks
170 from the German Weather Service (DWD) used for the uncertainty analysis, grouped in LS (short for long recording
171 stations)– tipping bucket sensors with 1min temporal resolution, 0.1mm accuracy, 2% uncertainty and observation lengths
172 from 40 -80 years, and in SS (short for short recording stations) – digital sensors with 1min temporal resolution, 0.01
173 accuracy, 0.02-0.04 mm uncertainty and observation length from 10-35 years. An overview of the data from these two
174 networks is given in Shehu et al. (2022). For both networks, the 1min time steps are aggregated to 5min and then Annual
175 Maximum Series (AMS) are extracted for each station for 12 durations levels from 5min to 7 days. To avoid the
176 underestimation of the rainfall depth due to fixed accumulation periods of 5, 10 and 15min, corrections factors of 1.14,
177 1.07 and 1.04 were used for the AMS of these durations according to the regulations in DWA-531 (DWA, 2012). Next,
178 as described in Shehu et al. (2022) a jump elimination according to sensor changes is performed (DVWK, 1999) in order
179 to ensure the stationarity of AMS at most stations for different duration levels.

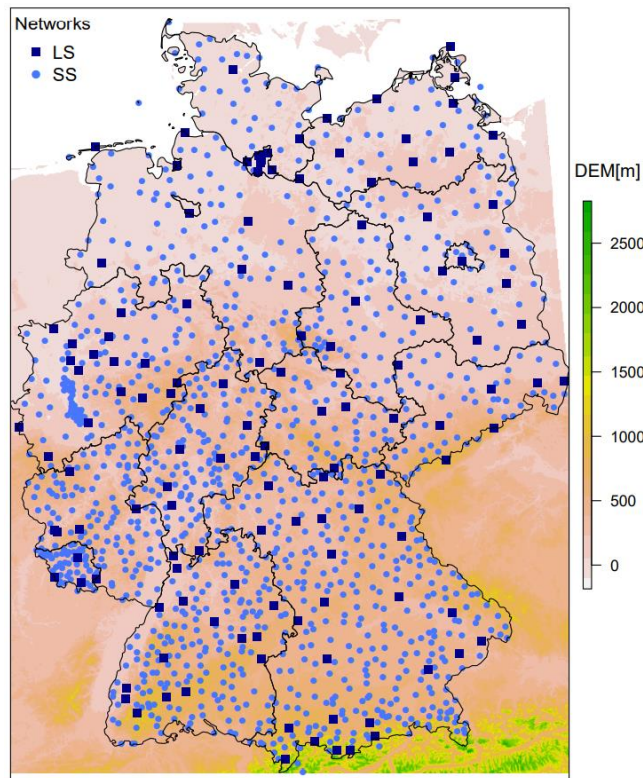


Figure 1 The distribution and location of the two rainfall networks used for the uncertainty analysis of Depth-Duration Frequency Curves in Germany: where LS represents the long and SS the short recording stations. DEM is short for digital elevation model (m) from SRTM (NASA Shuttle Radar Topography Mission SRTM, 2013).

2.1 Extreme Value Analysis

The local rainfall extreme value statistics describing the DDF curves for each station, are derived in two steps. First, the intensities of different duration levels are generalised according to the mathematical framework proposed by Koutsoyiannis et al. (1998) also illustrated in Equation (1):

$$i = i_d \cdot (d + \theta)^\eta, \quad (1)$$

where i is the generalised intensity in mm/h, i_d is the AMS intensity in mm/h at each duration, d is the duration in hours and θ, η are the Koutsoyiannis parameters optimised for each station. The optimisation of the Koutsoyiannis parameters is done by minimising the Kruskal-Wallis statistic. Second, a Generalized Extreme Value (GEV) distribution is fitted to the generalised intensities through the methods of the L-Moments (Asquith, 2021). The GEV is described by three parameters: location – μ , scale – σ , and shape – γ (with notation according to Coles, 2001) as given in Equation (2). For a robust estimation of extreme values with return periods of 100 years, the shape parameter was fixed at 0.1. The decision to fix the shape parameter at 0.1 was made based on existing literature and previous analysis that we have conducted on the data set in Germany. For more information regarding the choice of generalisation or shape parameter, the reader is directed to our previous study (Shehu et al., 2022). Keeping the shape parameter as fixed can be a reasonable choice to reduce the high uncertainty that is associated with the extreme values analysis at single stations. As shown in (Shehu et al., 2022), for return period higher than 20 years, the uncertainty from a free shape parameter is much higher than the uncertainty from keeping the shape parameter fixed at 0.1, which will cause the interpolation of extreme rainfall to be less certain.

$$F(x; \mu, \sigma, \gamma) = \exp \left\{ - \left[1 + \gamma \frac{(x + \mu)}{\sigma} \right]^{-\frac{1}{\gamma}} \right\}, \quad \gamma = 0.1 \quad (2)$$

Finally, the local statistics of each station are described by five parameters: three from the GEV distribution (μ, σ, γ) and two from the intensity generalisation over all durations (θ, η). Since the shape parameter is fixed at 0.1, only 4 parameters are regionalised independently from one another using kriging.

2.2 Direct Regionalisation (interpolation)

Here a spherical variogram is employed to describe the increment of the variance between any two points of observation situated at a specific distance h , as per Equation (3). The parameters of the variogram are estimated by of the methods of the least squares and human supervision.

$$\gamma(h) = c_0 + c \cdot \left(\frac{3h}{2a} - \frac{h^3}{2a^3} \right) \text{ for } h \leq a \text{ and } \gamma(h) = c \text{ for } h = a, \quad (3)$$

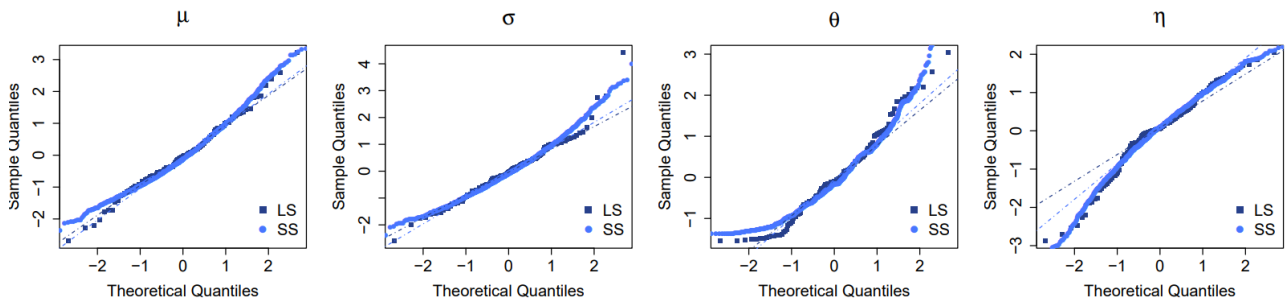
where c_0 is the nugget, c the sill and a the range of the variogram. Once the theoretical variogram is known, it can be used as a basis for regionalising the statistical properties on a 5x5km grid. The regionalisation (or the interpolation) with kriging is done in two steps, by considering independently the short (SS) and long (LS) recording stations. First, each of the SS parameters are interpolated with ordinary kriging (herein referred to as OK[SS]) based on the theoretical variogram of the SS dataset. Second, each parameter derived from the LS dataset is interpolated with external drift kriging KED[LS|SS] based on the theoretical variogram of LS dataset, whereas the OK[SS] serves as an external drift. The reason for this two-step procedure, is that the short recording stations have an inadequate length for estimating extremes of high return period, but still provide useful information about the spatial trends. For more information regarding the choice of this spatial regionalisation, the reader is directed to our previous study (Shehu et al., 2022).

216 **2.3 Data Transformation**

217 A requirement for the spatial simulations (Sequential Gaussian Simulation - SGS), is that the target variable to be
 218 interpolated (in this case each of the 4 parameters), should follow a normal distribution. Following the quantile-quantile
 219 plot, with sample vs normal quantiles, illustrated in **Figure 2**, it is clear that the dataset (both LS and SS) are not normally
 220 distributed, as the extremes (both lower and upper tail) deviate clearly from the normal distribution (the dashed continuous
 221 lines). Therefore, in case of a Sequential Gaussian Simulation (SGS) for assessing the spatial uncertainty, a transformation
 222 to normality is required. Deutsch and Journel (1998) propose a normal score transformation based on the empirical
 223 probabilities (Weibull plot position) as indicated in Equation (4).

$$224 \quad F(x)' = 1 - \left(\frac{k}{n+1} \right) \text{ and } x_{norm} = G^{-1}(F(x)'), \quad (4)$$

225 where $F(x)'$ is the empirical cumulative distributed function calculated based on the descending rank k of input data x , n
 226 is the number of available x -observation, G^{-1} is the inverse function of the gaussian distribution, and x_{norm} is the normalised
 227 input data.



228 **Figure 2** Sample quantiles of the 4 obtained parameters for both long (LS) and short (SS) datasets in comparison with the theoretical quantiles from the normal distribution. The dashed lines represent the normal quantile lines for a perfect fitting between the sample and the normal quantiles.

229 Respectively a back-transformation algorithm is also available to transform back the dataset from the normal to its original
 230 space. However, the back-transformation may be problematic as the tail behaviour will be underestimated by the normal
 231 score and back transformation. An alternative approach to the normal score transformation, is the fitting of the theoretical
 232 cumulative probability functions (CDF) to the original dataset, and perform the transformation from the chosen theoretical
 233 CDF to the normal one. Here, the problem of the choice for tail extrapolation is substituted with the choice of fitting a
 234 theoretical CDF. Through the method of L-Moments, different theoretical distributions were fitted to the available datasets,
 235 for instance the Wakeby distribution (WAK), the Weibull (WEI), the Generalized Normal (GNO) and the Generalized
 236 Extreme Value (GEV) probability distribution. For more information about the CDF and the fitting of the parameters, the
 237 reader is directed to Asquith (2021), Hosking and Wallis (1997). Afterwards the Cramer von Mises Goodness of Fit test
 238 (CSöRgö and Faraway, 1996) is performed to test whether or not the observed data belongs to the chosen theoretical CDF.
 239 The p-value statistics is used to compare the empirical CDF with the theoretical one for each dataset, in order to select
 240 the most adequate theoretical CDF. The results of the p-value statistics from Cramer von Mises Test are shown in **Table**
 241 **1**, and they reveal that the parameters of the long recording stations (LS) are better described by the WAK distribution,
 242 while the parameters of the short recording stations from the GNO distribution. All the parameters, except the $\theta_{[SS]}$,
 243 exhibit a very large p-value (higher than 0.90). Even though the p-value for $\theta_{[SS]}$ is 0.24, the null hypothesis that the
 244 theoretical distribution describes the current dataset can still not be rejected. To keep a consistent choice between the short
 245 and the long dataset, the GNO was chosen, as the best theoretical distribution for the SS and the second best for LS (shown
 246 in bold letters in **Table 1**).

Table 1 *p*-values of Cramer-von-Mises test for testing if the different theoretical distribution fits well to the data. The higher the value, the higher the certainty in accepting the null hypothesis that the chosen CDF describes correctly the data.

Long recording stations (LS)					Short recording stations (SS)				
CDFs	wak	wei	gno	gev	CDFs	wak	wei	gno	gev
$\mu_{[LS]}$	0.99	0.8	0.94	0.91	$\mu_{[SS]}$	0.77	0.68	0.99	0.99
$\sigma_{[LS]}$	0.96	0.8	0.9	0.85	$\sigma_{[SS]}$	0.85	0.39	0.980	0.95
$\theta_{[LS]}$	0.91	0.67	0.78	0.76	$\theta_{[SS]}$	0.24	0.15	0.24	0.2
$\eta_{[LS]}$	0.94	0.36	0.36	0.25	$\eta_{[SS]}$	0.52	0.83	0.91	0.27

247 A comparison of these two transformations, normal score according to Deutsch and Journel (1998) and the quantile-
 248 quantile transformation based on fitted theoretical distribution, was performed priority on a cross-validation mode for the
 249 SGS runs in ordinary kriging and external drift kriging. The results of such comparison favoured the quantile-quantile
 250 transformation based on fitted theoretical distributions.

251 2.4 Data Bi-Normality

252 An additional precondition to run the SGS and assess the spatial uncertainty is the multivariate normality. However as
 253 stated in Deutsch and Journel (1998), the data for checking multivariate normality (the tri-variate, quadrivariate and so
 254 on) are hardly enough to allow the interference of the corresponding experimental multivariate frequencies. Thus, they
 255 suggest that if the bivariate normality conditions are not violated, one can continue with the SGS experiments. Here the
 256 bivariate normality is tested by comparing empirical indicator variograms of the normalised parameters sets with the
 257 respective ones from a Bi-Gaussian random function that shares the same variogram with the normalised parameter sets.
 258 First, a theoretical variogram is fitted to the normalised observed variograms from dataset LS and SS (separately). Next
 259 the analytical relation given at Deutsch and Journel (1998) linking the covariance $C_Y(h)$ with any normal bivariate CDF
 260 value (with mean 0 and standard deviation 1).

$$261 \text{Prob}\{Y(u) \leq y_p, Y(u+h) \leq y_p\} = p^2 + \frac{1}{2\pi} \int_0^{\arcsin C_Y(h)} \exp\left(-\frac{y_p^2}{1+\sin\theta}\right) d\theta, \quad (5)$$

262 where y_p in the normal p -quantile of the normal bivariate CDF, and the $C_Y(h)$ is the correlogram obtained from normalised
 263 LS and SS dataset. For a given threshold y_p , the bivariate probability will be:

$$264 \text{Prob}\{Y(u) \leq y_p, Y(u+h) \leq y_p\} = E\{I(u;p) \cdot I(u+h;p)\} = p - \gamma_I(h;p), \quad (6)$$

265 with $I(u;p)$ equal to 1 for $Y(u) \leq y_p$ or equal to 0 if otherwise, and $\gamma_I(h;p)$ is the indicator variogram for the p -quantile
 266 (corresponding to threshold y_p) of the normal bivariate CDF. Three thresholds were chosen for the computation of the
 267 indicator variograms that corresponds to 0.25, 0.5 and 0.75 percentiles. Based on Equation (6), the generation of the Bi-
 268 Gaussian functions was performed of each set of data independently (short and long) with the GSLIB package. Lastly,
 269 the sample indicator variograms for the three thresholds are computed from the observed normalised datasets. The check
 270 consists in comparing for each threshold the empirical indicator variogram and the theoretical indication variogram from
 271 the normal bivariate CDF.

272 The obtained indicator variograms are shown in **Figure 3** for empirical data set (in points) and for the Bi-Gaussian
 273 functions (in solid lines) of the two datasets (short and long). From **Figure 3** it is visible that the Bi-Gaussian indicator
 274 variograms described well the empirical data sets for most of the cases. For instance, the θ and η parameters show a good
 275 agreement for the two types of indicator variograms. For the μ and σ parameters the agreement is better for the high
 276 thresholds than for the low one (0.25 percentile), where mainly the LS dataset differs more with the Bi-Gaussian indicator
 277 variogram than the SS dataset. To a certain degree this is expected, as the LS dataset is much smaller than the SS dataset.
 278 Overall, the Bi-Gaussian indicator variograms match well with the empirical ones, and the bivariate normality conditions
 279 are not violated. Hence, the SGS can be used for spatial simulation of the parameter sets.

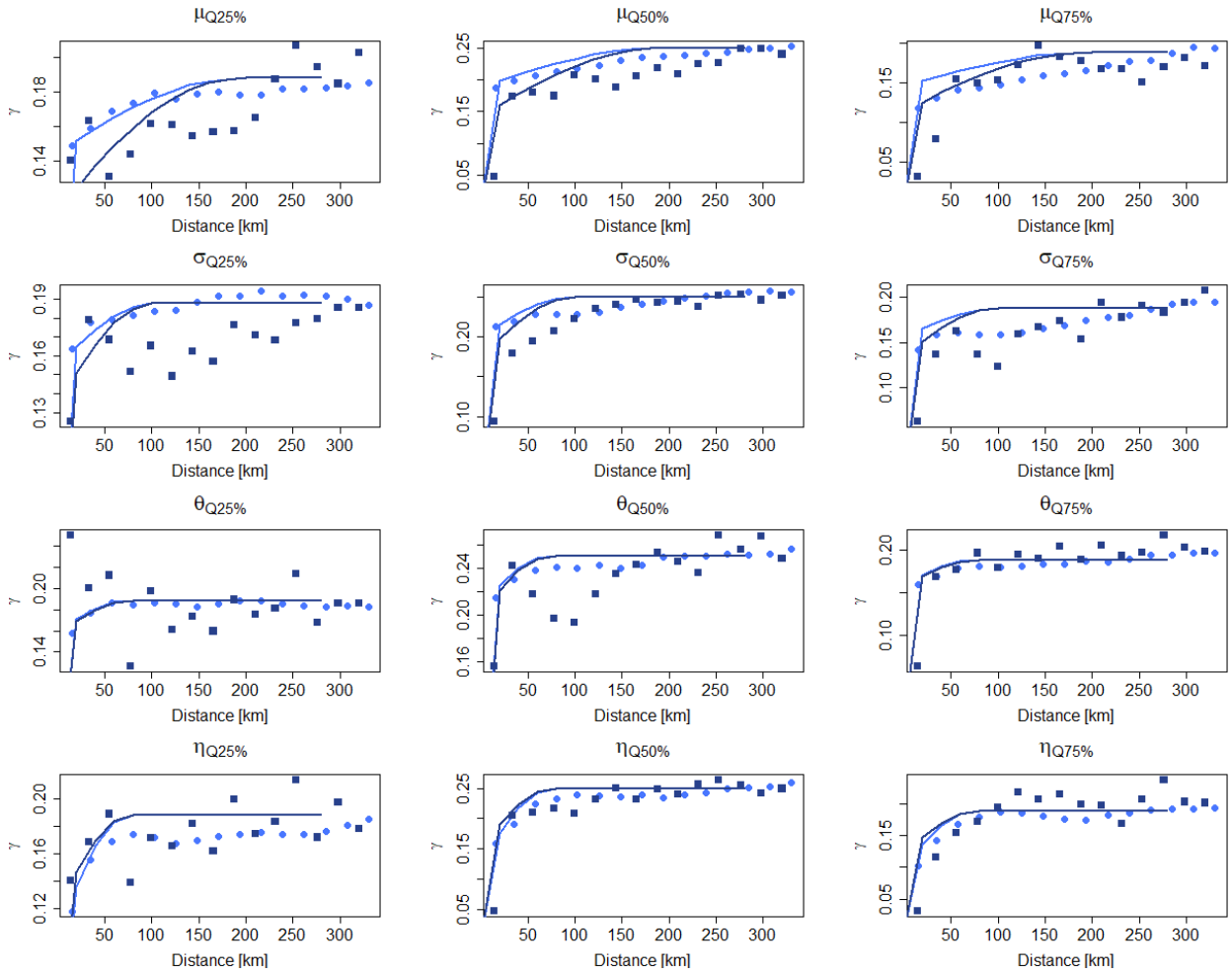


Figure 3 Experimental indicator variograms for the two datasets (SS in light blue, LS in dark blue) for the 4 parameters and their respective fits of the Bi-Gaussian model derived theoretical curves (shown respectively in solid line).

280

281 3. Methods for uncertainty estimation

282 The regionalisation of the four parameters describing the rainfall extreme value statistics, is performed using kriging, as
 283 the best regionalisation method from Shehu et al. (2022). The regionalisation is done primarily with the LS data and using
 284 the interpolation of SS parameters as an external drift. In this procedure, there are several sources of uncertainty that one
 285 should consider for the overall uncertainty, as illustrated in **Figure 4**, which are respectively:

- 286 • Sample uncertainty in estimating local extreme value statistics (four parameters), herein referred to as the local
 287 uncertainty.
- 288 • The uncertainty in the external drift which originates from the uncertainty in the estimation of the variogram
 289 based on the SS stations, and from the uncertainty in the regionalisation of the SS statistics. Here, only the latter
 290 is considered, as previous work revealed that this is more relevant than the former.
- 291 • The uncertainty in the regionalisation of the LS statistics originating from the estimated variogram from LS
 292 stations, and the uncertainty of the spatial regionalisation (herein referred to as spatial uncertainty).

293 Overall, the methodologies to tackle these uncertainties can be categorised in three main groups: the local estimation, the
 294 variogram estimation and the spatial simulation (as illustrated in blocks in **Figure 4**). The methodology for uncertainty
 295 estimation on each block is discussed accordingly in the following sections.

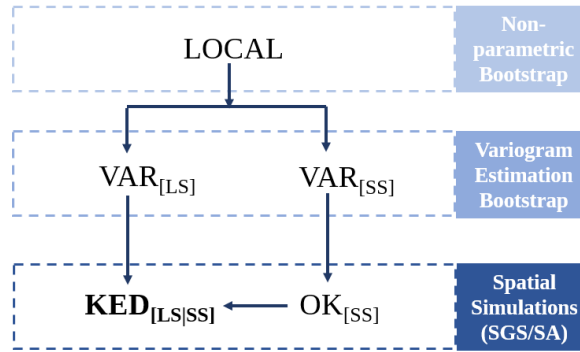


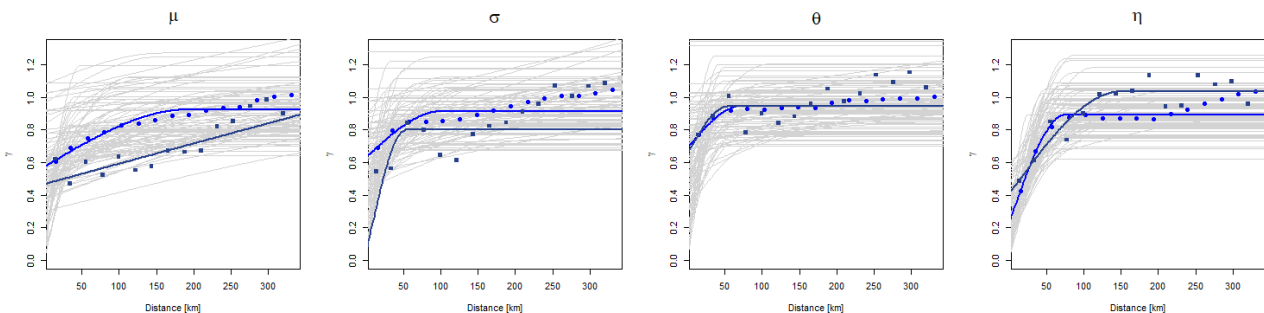
Figure 4 The main uncertainty sources in the regionalisation of the rainfall statistics for Germany for the selected methodology. Arrows indicate the calculation flow, and the blocks at the right represent the three main methodologies to tackle the uncertainty at each component.

297 **3.1 Local Non-Parametric Bootstrap**

298 A non-parametric bootstrap approach is implemented in order to quantify the sample uncertainty of the local rainfall
 299 extreme value statistics. This means that for each station the AMS are resampled with replacement for the same length of
 300 observations and the local statistics are then derived base on the methodology explained in Section 2.1. This resampling
 301 procedure is run 100 times for each location (either LS or SS), and for each time the parameters describing the local
 302 extreme value statistics are calculated. The resampled parameter-sets are then used as input for the rest of the
 303 regionalisation approach to first investigate the effect of the local uncertainty on the regionalisation output (results shown
 304 in Section 4.2) or their impact on the overall uncertainty of regionalised DDFs curves in Germany (results shown in
 305 Section 4.3).

306 **3.2 Variogram Simulations**

307 A non-parametric bootstrap is implemented in the variogram uncertainty, with the precondition that the spatial dependency
 308 between stations is maintained. The whole station dataset (both short and long recordings) are grouped together, from
 309 which 133 stations are sampled randomly 100 times. Only 133 values from all the stations were sampled here, to address
 310 the uncertainty in computing the variogram from a small dataset that corresponds with the number of the long recording
 311 stations that were used to compute the variogram for the KED interpolation. For each of the sample, first the empirical
 312 variogram is calculated and then a theoretical spherical one is fitted automatically. Such sampling of variogram, is
 313 indirectly accounting the low station density and the short observation length for the final interpolation of KED[LS|SS].
 314 The obtained variogram simulations are shown in **Figure 5**. For each of the estimated variogram, the kriging interpolation
 315 is performed and in the end its effect on the final regionalisation output is discussed in Section 4.2.



316

Figure 5 100 variogram realisations obtained from bootstrapping (shown in grey lines) the station datasets, the empirical variograms as observed by the normalised LS (in dark blue points) and SS database (in light blue points), and the respective fitted theoretical spherical variograms used for the interpolation.

317 3.3 Spatial Simulations

318 The uncertainty in the spatial regionalisation is assessed by generating 100 equiprobable realisation of the normalised
319 parameter sets, where each realisation is honouring the global statistics of the parameter (the spatial mean value and the
320 variogram). Here a conditional simulation is performed, where these 100 realisations do not only share the global statistics
321 but as well a set of observed values at certain locations. In other words, for the known locations where there are
322 observations, either the nodes are not resampled (as in the case of simulated annealing) or the nodes are allowed to vary
323 according to the variogram nugget when compared to the observations (as in the case of the sequential Gaussian
324 simulation). The spatial simulations are conditioned to the location of the 133 long recording stations (LS) since they are
325 the main input for the regionalization are considered the ground truth.

326 3.3.1 Sequential Gaussian Simulation (SGS)

327 The Sequential Gaussian Simulation (SGS) is the most straight forward algorithm for generating such equiprobable
328 realisation and it is proven to be more robust than other algorithms (Pebesma and Wesseling, 1998). An overview of this
329 procedure, where a normal continuous variable $z(u)$ is modelled by a Gaussian stationary random function $Z(u)$ is
330 described as follows (Deutsch and Journel, 1998):

- 331 1. A random path is defined that is visiting each node of Germany grid (at 5km² spatial resolution) once. At each
332 node u , fix the neighbouring conditional locations (either SS for OK[SS] and LS for KED[LS|SS]) and their
333 observed values z , as well as the previously simulated z values at the grid node.
- 334 2. Do either ordinary kriging with the normalised short recording stations (OK[SS]) or kriging with external drift
335 with the normalised long recording stations (KED[LS|SS]) using the respective variograms to estimate the global
336 statistics (mean as per Equation (7) and variance as per Equation (8)) of the Conditional Cumulative Distribution
337 Function (CCDF) at the random function $Z(u)$ at the location u .

$$338 \mu(u) = \sum_{i=1}^n \lambda_i \cdot Z(u_i), \quad (7)$$

$$339 \sigma^2(u) = C(0) - \sum_{i=1}^n \lambda_i \cdot C(u - u_i), \quad (8)$$

340 where λ_i are the weights as estimated by ordinary kriging for OK[SS] and kriging with external drift for
341 KED[LS|SS], $Z(u_i)$ is the conditional value of the target variable at the u_i location, with i corresponding to
342 conditional values in the neighbourhood (within a maximum radius of 300km and within the range 12 to 24),
343 $C(0)$ is the variance and $C(u - u_i)$ the covariance of the normalised dataset.

- 344 3. Draw randomly a value from this CCDF as $z'(u)$ and add this simulated value to the conditional dataset.
- 345 4. Proceed to the next node, until all nodes are simulated.

346 The “gstat” package available in R is used to generate such realisation both for the ordinary kriging interpolation of the
347 SS database (OK[SS]) and for the external drift kriging interpolation of the LS database (KED[LS|SS]) (Pebesma, 2004).
348 Note that the spatial simulations are always performed on the normal space (normal transformation of the dataset). For
349 the simulation of the KED[LS|SS] both the input dataset LS and the external drift OK[SS] are as well in the normal space.
350 A back-transform to the original space is done after each spatial simulation only for the final product KED[LS|SS].

351 3.3.2 Simulated Annealing Simulations (SA)

352 Simulated Annealing is an alternative method for generation conditional stochastic images. New images are created by
353 randomly selected values from the observed histograms, such that global statistics like variogram, marginal distribution,
354 correlation to a secondary variable are maintained. Unlike the SGS method, no prior assumption of normality is needed,
355 and hence the observed data (with no prior transformation) can be directly used. An overview of this procedure is found
356 in (Deutsch and Journel, 1998) and also explained shortly below:

- 357 1. An initial image is randomly created by the observed histogram. For nodes where data is observed, the random
 358 values are substituted by the observed ones. Thus, the observed values are exactly reproduced. This image
 359 matches the observed histogram and conditional data, but not the observed variogram.
 360 2. An objective function is calculated, and a conditional simulation is reached when the objective function is as
 361 close as possible to zero. For generation of the external drift spatial information (OK[SS]) only the variogram is
 362 used as part of the objective function, while for the final parameter estimation (KED[LS|SS]) additionally the
 363 correlation with the external drift is preserved.

$$364 \quad OF_{OK[SS]} = w_1 \sum_h \frac{[\gamma'(h) - \gamma(h)]^2}{\gamma(h)^2}, \text{ and } OF_{KED[LS|SS]} = w_1 \sum_h \frac{[\gamma'(h) - \gamma(h)]^2}{\gamma(h)^2} + w_2 [\rho' - \rho]^2 \quad (9)$$

365 where $\gamma'(h)$ is the simulated variogram, $\gamma(h)$ the observed variogram, ρ' the simulated correlation and ρ the
 366 observed correlation with the external drift, w_1 and w_2 are weights for the two components (both equal to 5).

- 367 3. If the value of the objective function is not reached, a new image is created by swapping randomly values of pair
 368 nodes (not conditioned nodes), and the objective function is recalculated.
 369 4. If the new objective function is better than the previous one (closer to zero), then the swap is accepted, if not the
 370 swap is accepted based on an exponential probability distribution. The parameter of the exponential probability
 371 distribution is equal to the temperature in simulated annealing.

$$372 \quad Prob_{.accept} = \begin{cases} 1, & \text{if } OF_{new} \leq OF_{old} \\ e^{\frac{OF_{old} - OF_{new}}{t}}, & \text{otherwise} \end{cases} \quad (10)$$

373 where $Prob_{.accept}$ is the acceptance probability distribution, t is the temperature (which decreases with each
 374 iteration), OF_{new} is the new objective function obtained by swapping a pair of values and OF_{old} is the previous
 375 objective function value. As higher the temperature, the higher the probability to selected such unfavourable
 376 swaps.

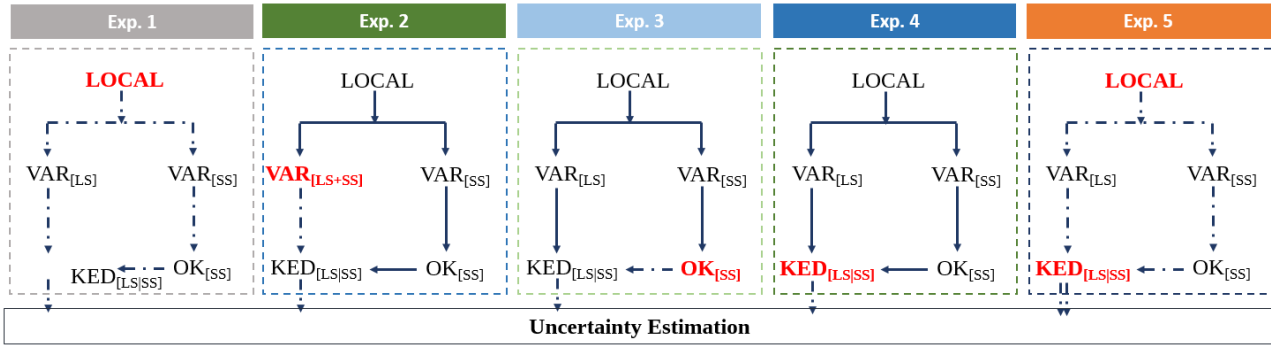
- 377 5. Redo step 3-4, until a maximum number of swaps is reached, or if a maximum number of accepted swaps is
 378 reached. If this is the case, the temperature t is reduced by a multiplicative factor Ω (here as 0.1).
 379 6. Redo steps 3, 4, and 5 until convergence is reached or if the maximum number of possible swaps is reached S
 380 times. The simulation is then completed and the image is frozen.

381 The ‘‘GSLIB’’ program from (Deutsch and Journel, 1998) was employed to generate 100 random realisation fields for
 382 both the external drift and the interpolation. Note two main differences of the SA with SGS: i) no data transformation and
 383 back transformation is required, ii) by fixing a seed number, the random path in SGS is same for all the parameters, while
 384 for the SA the random path for each parameter depends on how fast the optimum criteria is reached.

385 3.4 Uncertainty Estimation and Propagation

386 Based on several simulations, the uncertainty is evaluated only at the locations on the long recording stations (LS) – in
 387 total 133 stations. Different experiments are conducted in order to investigate first how the sources of uncertainty are
 388 propagating to the final regionalisation of the 4 parameters (experiments 1-4), and how the main sources of uncertainty
 389 are interacting with each other to produce the total uncertainty (experiment 5). An overview of these experiments and the
 390 sources of uncertainty they consider, is given in **Figure 6** and in **Table 2**. Note that in experiment 5, two uncertainty
 391 sources are combined: the local uncertainty from the sampling of rainfall extreme value statistics and the spatial
 392 uncertainty from KED[LS|SS] simulations. This means that at experiment 5 for each realisation of the local statistics,
 393 both variograms of LS and SS are re-calculated, the OK[SS] is derived and respectively 100 KED[LS|SS] simulations are
 394 generated, concluding thus in a total of 10,000 simulations. The bootstrapping of the variograms (VAR[LS|SS]) is left
 395 outside of this experiment, because as it is shown in section 4.2, doesn’t have a major impact on the regionalisation output.

396 Moreover, as the variograms are re-estimated, different variograms are as well modelled, including the variogram
 397 uncertainty indirectly. Here only the combination of local and spatial uncertainty at KED[LS|SS] simulations are included
 398 as prior work revealed that this produces the highest uncertainty in terms of precision.



399 **Figure 6** Different experiments run for the propagation of the uncertainty. The red bold letters indicate the source of
 uncertainty investigated for each experiment and how it propagates throughout the regionalisation procedure (in dashed
 arrows). The number of arrows at the experiment 5 indicate different uncertainty sources combined together.

Table 2 The description of the uncertainty propagation for each of the experiments shown in **Figure 6**, and the number
 of realisations considered for each experiment.

Exp.	Explanation	No. of realisations
1	For each local re-sampled extreme value statistics, the regionalisation procedure is run.	100
2	For each variogram estimated from LS+SS database, the regionalisation procedure is run.	100
3	For each spatial realisation of the OK[SS], the regionalisation procedure is run.	100
4	For each spatial realisation of the KED[LS SS], the regionalisation procedure is run.	100
5	For each local re-sampled extreme value statistics and spatial realisation of KED[LS SS] the regionalisation procedure is run.	10,000

400 For each of these experiments, the final regionalisation step of the 4 parameters (KED[LS|SS]) is run on a cross-validation
 401 mode: which means that each of the LS station is left stepwise outside of the database, and the remaining database is used
 402 to estimate this LS location. The simulations at the LS stations are then used as a basis for the uncertainty estimation of
 403 each parameter separately, and for the final rainfall depth (RD) obtained at specific return periods (T1a, T10a and T100a)
 404 and 12 duration intervals (5, 10, 15, 30, 60, 120, 180, 360, 720, 1440, 2880, 7340 mins). For each LS location, the
 405 uncertainty is estimated based on the experiment simulations using the following criteria:

406 Normalised 95% Confidence Interval Width: $nCI95_{width} [\%] = 100 \frac{x_{97.5\%} - x_{2.5\%}}{\bar{x}}$, (11)

407 where x represents the simulations of the target variable at a specific location, $x_{97.5\%}$ and $x_{2.5\%}$ are the respective 97.5%
 408 and 2.5% quantile of the x simulations, and \bar{x} is the expected value of x from the simulations of an experiment. The
 409 normalised 95% Confidence Interval Width ($nCI95_{width}$) is a measure of spatial simulations precision: the smaller the
 410 value, the more robust or precise is the estimation method for x .

411 Average Error over all simulations: $Bias [\%] = 100 \frac{\sum_{sim=1}^{nsim} (x_{sim} - x_{obs})}{nsim}$, (12)

412 where x represents the simulation of the target variable at a specific location from the random simulation sim , x_{obs} is the
 413 local observed target variable at the specific location, and $nsim$ represent the total number of simulations for each
 414 experiment. The average error over all the simulations measures the accuracy of the realisation compared to local input

415 data. When rainfall depth (RD) is the target variable, one can go one step further and measure how well the realisations
 416 capture the monotonically increase of the RD at different duration intervals for specific return periods, which corresponds
 417 to the evaluation criteria in estimating the best regionalisation method for Germany on our previous study (Shehu et al.,
 418 2022).

$$419 \quad \text{Percentage RMSE:} \quad RMSE_{st,Ta}[\%] = 100 \cdot \frac{\sqrt{\frac{1}{D} \sum_{d=1}^D (RD_{regio,d} - RD_{local,d})^2}}{\overline{RD_{local}}}, \quad (13)$$

420 where Ta and st are the respective selected return period and LS location, RD_{regio} corresponds to the regionalised rainfall
 421 depth (with KED[LS|SS]), RD_{local} the locally derived rainfall depth from the normalised GEV function (from Equation
 422 (1) and (2)), the $\overline{RD_{local}}$ is the mean local rainfall depth over all duration levels, and the d is an index indicating the
 423 iteration from 1st to D=12th duration interval. Through the Equations (12) and (13) and the cross-validation mode, it is
 424 possible to compare the performance the simulations with the direct regionalisation (i.e. interpolation) from Shehu et al.
 425 (2022), in order to investigate if the simulation methods are appropriate.

426 **4. Results and Discussion**

427 **4.1 Comparison of different models in modelling spatial uncertainty**

428 Before analysing the propagation of different uncertainty sources, the best method for computing the spatial uncertainty
 429 is investigated. As discussed in Section 3.3 two methods are employed for the generation of 100 equiprobable realisations
 430 both for the drift information (OK) and the interpolation of the long recording stations with external drift kriging (KED):
 431 the Sequential Gaussian Simulation (SGS) as method 1 and the Simulated Annealing (SA) as method 2. **Figure 7**
 432 illustrates the parameter precision (nCI95_{width} [%]) and accuracy (Bias [%]) of these 100 simulations calculated in cross-
 433 validation mode for each of the long recording locations (in total 133) for both methods. Note that the transformation to
 434 normality is required only for the SGS and not the SA simulations, as the SA simulations are performed based on observed
 435 histograms. The main differences between the two simulation methods are seen in the precision obtained from the 100
 436 realisations (nCI95_{width} – upper row), where the realisations from the SA approach are more precise than the ones from
 437 the SGS approach. The difference in the precision is much higher in the KED[LS|SS] than for the OK[SS] for all the 4
 438 parameters. In terms of parameter accuracy, both methods have similar performance for both OK[SS] and KED[LS|SS],
 439 with SA having slightly higher errors than the SGS and the direct regionalisation (i.e. interpolation) performance
 440 (particularly for the μ and θ parameter). Overall it seems that the SA is more precise than the SGS, nevertheless as the
 441 focus is on Depth-Duration-Frequency curves, the methods should be as well compared in their ability to estimate the
 442 DDF curves. For this purpose, for each cross-validation location, the RMSE [%] was first calculated as per Equation (13)
 443 for each simulation, and then the median over the 100 simulations was obtained. The median RMSE [%] performance for
 444 different return periods for both methods are shown in **Figure 8**. The median RMSE [%] performance obtained by the
 445 SGS method seems to be in accordance with the performance of the direct regionalisation (interpolation) for both OK[SS]
 446 and KED[LS|SS]. In contrast, the RMSE [%] performance from the SA simulations are slightly worse than the direct
 447 regionalisation for OK[SS], and much worse for the KED[LS|SS] over all return periods (median up to 5-8% higher).
 448 Even though the SA produces more precise simulations of parameters, it fails to maintain the inter-relationship between
 449 the parameters, causing lower accuracy in the DDF estimation. The SGS on the other hand, keeps the same level of
 450 accuracy like the direct regionalisation (interpolation) but with a lower precision. Since the aim is to keep accuracy as in
 451 the direct regionalisation (interpolation), SGS was chosen as a more suitable method to model the spatial uncertainty.

452 Also, since the SGS produces a higher range of simulations, the estimated precision, in the end, is more conservative than
 453 the SA procedure.
 454

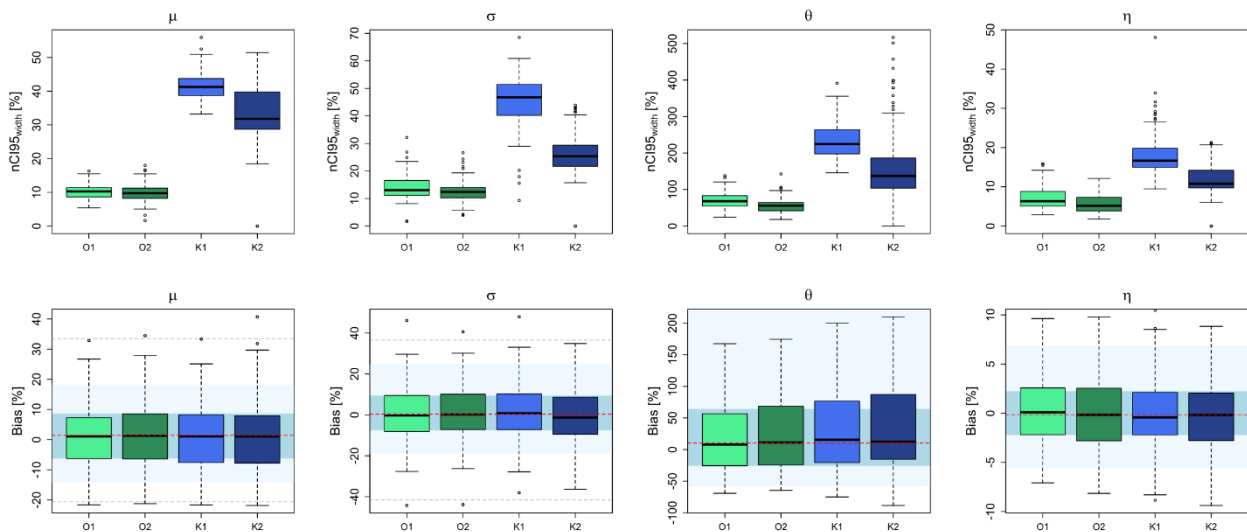


Figure 7 The precision ($nCI_{95_{width}}$ [%]) and accuracy (Bias [%]) of two different spatial simulations methods (1-SGS and 2-SA) for the drift regionalisation (O) and final regionalisation (K) of the 4 parameters. The boxplots illustrate the performance over the 133 LS locations. The background shades in the lower row illustrate the accuracy of the direct regionalisation (i.e. interpolation) of observed local statistics in a cross-validation mode, where: red dash indicates the median accuracy over all stations, the blue region the inter-quantile range (IQR) of all stations, the light blue region the 95% and 5% quantiles, and the grey dashed lines the maximum and minimum performance over all stations.

455

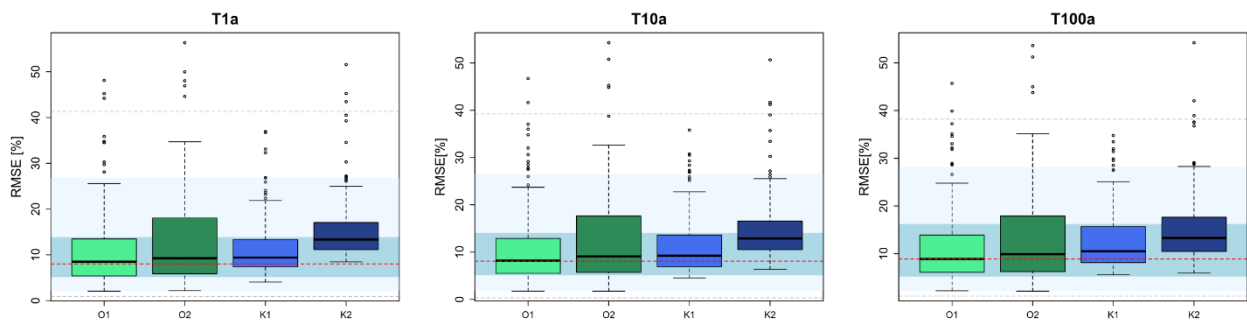


Figure 8 The accuracy (RMSE [%]) of two different spatial simulations methods (1- SGS and 2 - SA) for the drift regionalisation (O) and the final regionalisation (K) of the Depth-Duration-Frequency curves. The boxplots illustrate the median RMSE over the 133 LS locations. The background shades illustrate the accuracy of the direct regionalisation (i.e. interpolation) of observed local statistics in a cross-validation mode, where: red dash indicates the median accuracy over all stations, the blue region the inter-quantile range (IQR) of all stations, the light blue region the 95% and 5% quantiles, and the grey dashed lines the maximum and minimum performance over all stations.

4.2 Effect of different uncertainty components for the estimation of the DDF Curves at ungauged locations

456 Experiments 1 to 4 were conducted in order to investigate the uncertainty propagation from each component of
457 regionalisation to the final parameter and DDF values, while Experiment 5 considers a propagation of the two main
458 uncertainty sources interacting together in the final regionalisation of the extremes. The parameter uncertainty is
459 calculated from the number of simulations given in **Table 2** for each experiment, and is illustrated in **Figure 9**; where the
460 upper rows represents the precision ($nCI95_{width}$ [%]), while the lower rows the accuracy (Bias [%]) of estimated parameters
461 in a cross-validation mode. **Figure 10** illustrates the DDF uncertainty at duration levels from 5min up to 7 days for three
462 return periods 1, 10 and 100 years: precision ($nCI95_{width}$ [%]) shown in upper row and accuracy (RMSE [%]) at the lower
463 row. The accuracy of the simulations is compared with the direct regionalisation (i.e. interpolation) of the observed
464 parameter sets (see caption for more details). It is worth mentioning that the difference between the different component
465 simulations (Experiment 1 to 4) is visible only at the precision of the simulations and not at the accuracy. As illustrated
466 by **Figure 9**– lower row and **Figure 10**– lower row, the accuracy at estimating the parameters (Bias [%]) and the DDF
467 values (RMSE [%]) is not changing considerably from one experiment to the other. Also, when comparing the boxplots
468 with the performance obtained from the direct regionalisation (interpolation - shown with the background colours), the
469 same accuracy more or less is observed. Therefore, the analysis will be focused on the variation of precision ($nCI95_{width}$
470 [%]) according to different sources of uncertainty. Regarding the parameter uncertainty as shown by **Figure 9**, the spatial
471 KED[LS|SS] simulations (Exp. 4) represent the highest source of uncertainties for all the parameters: the $nCI95_{width}$ [%]
472 ranges from 18% for the η parameter, between 40-50% for the two GEV parameters μ and σ , and up to 250% for the θ
473 parameter. The parameters are varying greatly in space, and that is why when sampling from space (spatial simulations)
474 the prediction intervals are higher than for the bootstrapping case (or the other cases). For all the parameters, the $nCI95_{width}$
475 of the KED[LS|SS] simulations are at least 3 times higher than the $nCI95_{width}$ of the other uncertainty sources, concluding
476 that the spatial simulations add to the regionalisation the biggest uncertainty. Second to the KED[LS|SS] simulations, are
477 the resampling of local statistics (Exp. 1) and the OK[SS] simulations (Exp. 3), which seems to produce similar levels of
478 $nCI95_{width}$ for most parameters ranging from 10% for the location - μ , 90% for the θ and only 8% for the η parameter.
479 Only for the scale GEV parameter (σ) is the $nCI95_{width}$ from the local statistics resampling higher (~20%) than the one
480 from OK[SS] (~15%). It is interesting to see, that the obtained $nCI95_{width}$ from the variogram bootstrapping (Exp. 2) are
481 lower than 5% for almost all parameters (exception θ parameter which is lower than 20%). This suggests that the
482 variability between interpolated fields with different variograms is reproducing very similar spatial parameters, even
483 though the variograms differ greatly in terms of nugget, sill and range (see **Figure 5**). The same behaviour is also seen in
484 estimated DDF curves for different return periods (**Figure 10** – upper row), where the variability as exhibited by the
485 variogram bootstrapping (Exp. 2) is very low (less than 10%) compared to the other simulations, and as well constant
486 over the duration levels. On the other hand, the simulations from both local resampling (Exp. 1) and OK[SS] simulations
487 (Exp. 2) exhibit similar patterns of $nCI95_{width}$ for the selected DDFs curves (**Figure 10** – upper row). Unlike the $nCI95_{width}$
488 exhibited at the parameter simulations, here it is more visible the difference between these two components, as the $nCI95_{width}$
489 produced by the local resampling (Exp.1) are 1-5% higher than the one produced by the OK[SS] simulations (Exp.3). As
490 seen also in **Figure 10** – upper row, the $nCI95_{width}$ from the KED[LS|SS] (Exp. 4) are the highest compared to the other
491 components, emphasizing that the spatial uncertainty of the KED[LS|SS] is the main source of uncertainty when
492 regionalising the DDF curves. Also, unlike the other types of uncertainties (Exp. 1 to 3), the spatial uncertainty from the
493 KED[LS|SS] depends greatly on the duration level, with $nCI9_{width}$ values of short duration intervals (from 5min up to 2
494 hours) being considerably higher than the other experiments (reaching on average values of 40%). Moreover, Exp. 4
495 boxplots are much wider than Exp. 1 to 3, suggesting that the spatial uncertainty is highly dependent on the location. The
496 high uncertainty values in terms of precision for Exp. 4, come with the cost of slightly increased error in RMSE (**Figure**
497

498 **10** -lower row), where the median RMSE values are 1-2% higher than those of the direct regionalisation, but still within
 499 the Inter-Quantile-Range (IQR) of the direct regionalisation performance.

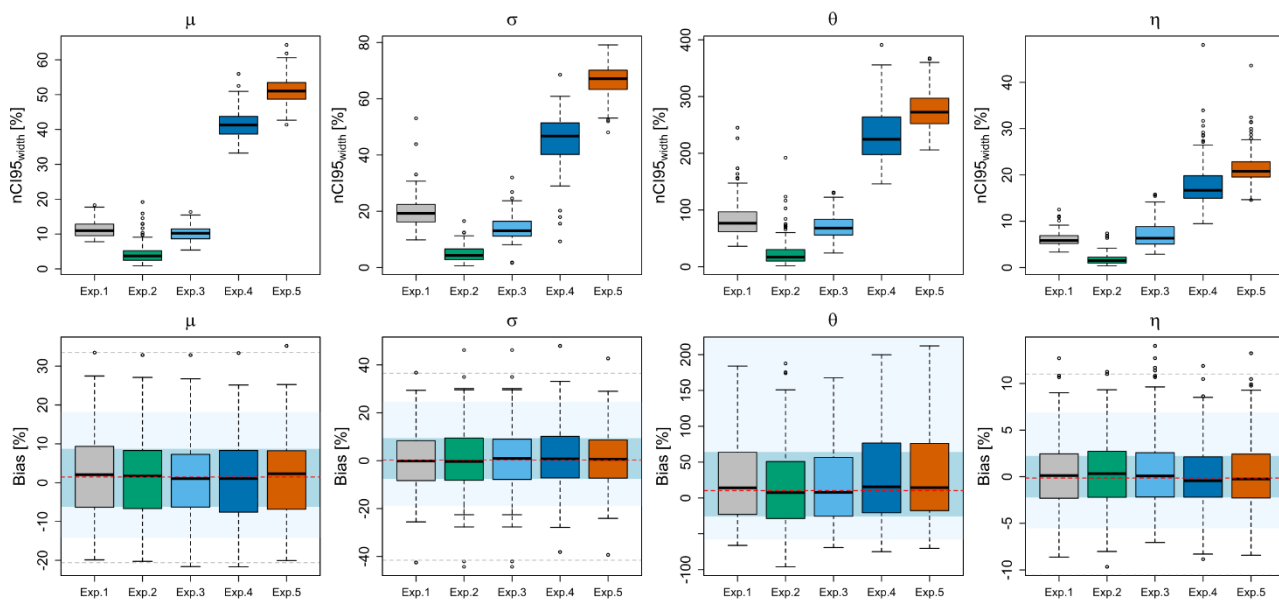
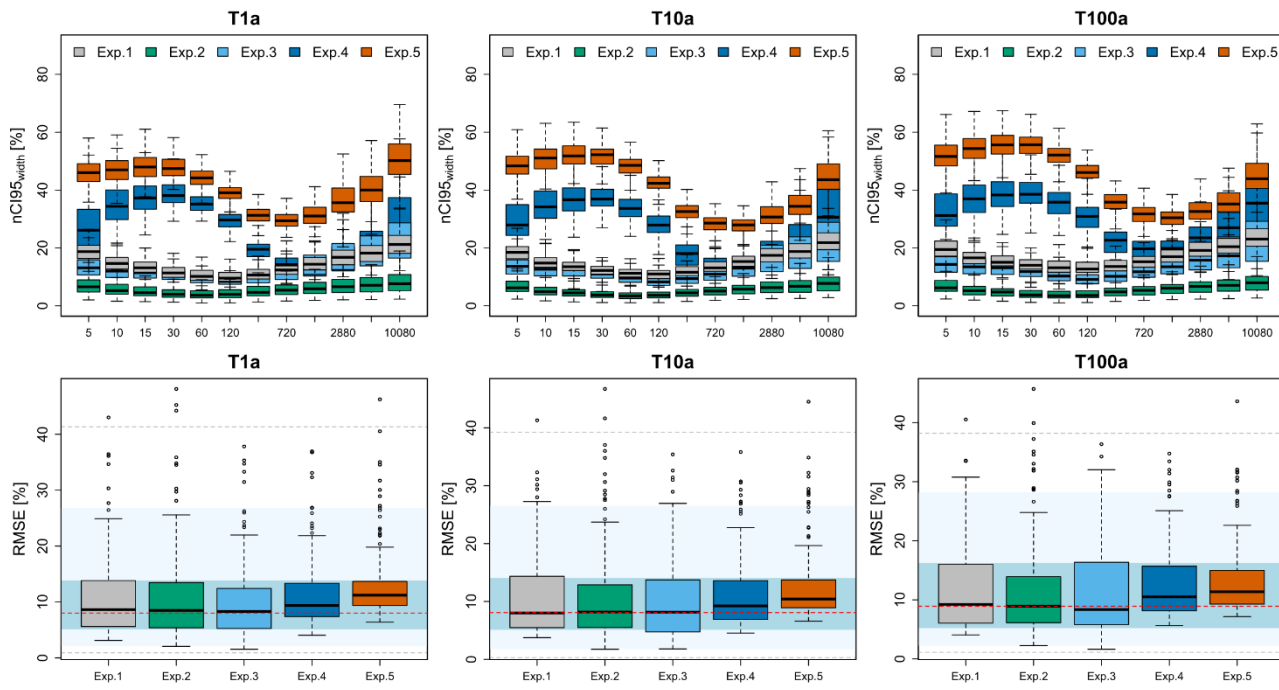


Figure 9 The obtained precision (first row - $nCI95_{width}$ [%]) and accuracy (lower row - Bias [%]) from propagating the multiple realisations at different components of the regionalisation procedure to the final parameter sets. The background shades in the lower row illustrate the accuracy of the direct regionalisation (i.e. interpolation) of observed local statistics computed as well in a cross-validation mode, where: red dash indicates the median accuracy over all stations, the blue region the inter-quantile range (IQR) of all stations, the light blue region the 95% and 5% quantiles, and the grey dashed lines the maximum and minimum performance over all stations.

500



501

Figure 10 The obtained precision (first row - $nCI95_{width}$ [%]) and accuracy (lower row - RMSE [%]) from propagating the multiple realisations at each component of the regionalisation procedure to the final DDF values. The background shades in the lower row illustrates the accuracy of the direct regionalisation (i.e. interpolation) of observed local statistics computed as well in a cross-validation mode, where: red dash indicates the median accuracy over all stations, the blue

region the inter-quantile range (IQR) of all stations, the light blue region the 95% and 5% quantiles, and the grey dashed lines the maximum and minimum performance over all stations.

502 So far, the experiments 1 to 4 considered the propagation of singular uncertainty sources to the final regionalisation of
503 parameters and DDF curves in Germany. Experiment 5 considers a propagation of the two main uncertainty sources
504 interacting together in the final regionalisation of the DDF curves. As stated before, the most important sources are; the
505 local estimation of rainfall extreme statistics, and the spatial uncertainty in regionalisation (KED[LS|SS]). As the
506 variogram and the external drift is calculated for each local resampling dataset, the uncertainty of variogram and external
507 drift is already included in the propagation of uncertainty from local resampling to spatial simulations. For each of the
508 two components, 100 realisations are run, resulting in a total of 10,000 simulations. Overall, the final and total uncertainty
509 from Exp. 5 follows a similar pattern to the uncertainty from KED[LS|SS] simulations, but due to the local uncertainties,
510 it manifests higher values of $nCI95_{width}$ and RMSE (as seen in **Figure 9 and 10**). The variation of the total $nCI95_{width}$ for
511 almost all parameters is 10-20% higher than those of Exp.4, with the GEV parameters reaching values of 50% (μ) to 70%
512 (σ), the θ parameter up to 270% and the η parameter up to 20%. Consequently, the variation of the total $nCI95_{width}$ over
513 the duration levels is between 35-50% for return periods 1 and 10 years and between 40-80% for return period of 100
514 years. As with the KED[LS|SS] simulations (Exp. 4), the durations shorter than 120min and the ones longer than 3 days,
515 exhibit higher $nCI95_{width}$ values, with the durations from 6 – 48 hours having the highest precision (lowest $nCI95_{width}$
516 values). Another property seen from experiment 5 is that the variation in space (the wideness of boxplots) is narrower
517 than in Exp. 4 for most of the durations, suggesting that the final spatial uncertainty is more constant in space (inheriting
518 a property from local uncertainty – Exp. 1). In term of accuracy, the RMSE [%] has been increased on average with 3%
519 for 1-year return period, and to 4-5% for 10-100 years return periods, differing slightly from the direct regionalisation
520 (i.e. interpolation) performance, but still within the Inter-Quantile-Range (IQR) of the direct regionalisation. Some
521 outliers are present in the accuracy plot (lower row **Figure 10**), however expect for one location, these outliers are within
522 the maximum RMSE manifested by the direct regionalisation. The behaviour of these outliers emerges both from
523 parameter outliers and from looking at the quantiles. They are present at locations where parameters are considerably
524 different from the neighbour long observations (as in the case of singular stations in the Black Forest or the Alps), or
525 where a parameter outlier is located (as in the case of Münster City where a very rare extreme event in 2014 causes a high
526 value for the scale σ parameter) and are not geographically clustered. Since the median of the simulations from
527 experiments 5 is increasing slightly the RMSE [%] but still within the IQR of the direct regionalisation, the simulations
528 can be used to quantify the total uncertainty range for the regionalisation of the Depth-Duration-Frequency Curves. Under
529 this context, the $nCI95_{width}$ [%] values in **Figure 10** can be divided by two, to show the tolerance range above or below
530 the predicted values at each node from the direct regionalisation. For instance, if at a specific location, for duration of
531 5min and return period 100 years, the simulated $nCI95_{width}$ [%] is 40%, which means that the regionalised rainfall depth at
532 this location is varying with $\pm 20\%$ of its mean value.

533 A parabolic relationship is visible for experiments 1-3, with lower $nCI95_{width}$ values at the mid-duration levels (1 and 2
534 hours) and increasing values at lower and longer durations. This parabolic behaviour over the different duration levels is
535 attributed to the Koutsoyiannis framework for generalising the intensities over all durations by the two parameters θ and
536 η . A particular behaviour is the variation of the $nCI95_{width}$ over the DDF values from the KED[LS|SS] simulations (Exp.
537 4), which is inherited as well at the final uncertainty computation (Exp. 5). The behaviour exhibited by KED[LS|SS]
538 simulations does not follow a parabolic function as in Exp. 1, Exp. 2 and Exp. 3, but more a sinusoidal one. This can be
539 attributed to two main reasons: 1. The effect of the Koutsoyiannis parameters on different durations, and 2. The spatial
540 simulations of the SGS algorithm following the transformation to normality.

541 **Figure 11** – upper row illustrates the observed empirical and simulated CDF from Exp. 4 for each parameter extracted
 542 from the LS dataset. Overall the simulated CDFs agree well with the observed CDFs, however the tails might diverge
 543 slightly. This is particularly true for the lower tail of the θ and η parameters, and the upper tail of the σ parameter. This
 544 occurs as the transformation is done on a continuous CDF, a GNO is first fitted to the data and based on the GNO-CDF
 545 the transformation is performed. Nevertheless, this is not negative, as like this, values outside the observed range are
 546 simulated, and hence higher or lower values can be simulated as well. As stated in (Marra et al., 2019b), the rainfall
 547 stations will not capture the maximum intensities of a storm, and thus is almost certain that they don't represent the high
 548 possible intensities. Therefore, generating higher or lower parameter values than observed is crucial in the generation of
 549 stochastic simulations. **Figure 11** – lower row illustrates the correlation between pairs of LS parameters (shown in red
 550 dots), and the corresponding correlations obtained from the 100 KED[LS|SS] simulations run in the cross-validation mode.
 551 For the μ - σ pair the observed correlation is well captured as it coincides with the median of the simulations. To a certain
 552 degree, this is also true for the θ - η pair. The main differences are in the relationships between the GEV and Koutsoyiannis
 553 parameters, where the simulated correlation is much higher than observed. In particular the correlation between μ , σ , and
 554 θ are higher than the correlation between μ , σ , and η . This explains why the precision of the KED[LS|SS] has a sinusoidal
 555 behaviour. The fluctuation of the θ parameter is affecting the uncertainty of the short durations (mainly from 5 to 60min),
 556 while the fluctuation of the η parameter affects the uncertainty at short (5-30min) and very long durations (12hours to 7
 557 days). Since the θ parameter is highly correlated with the μ and σ parameters, its fluctuations will result in a smaller
 558 uncertainty than the η fluctuations, resulting in a slight increase of precision between the duration of 5-30mins.

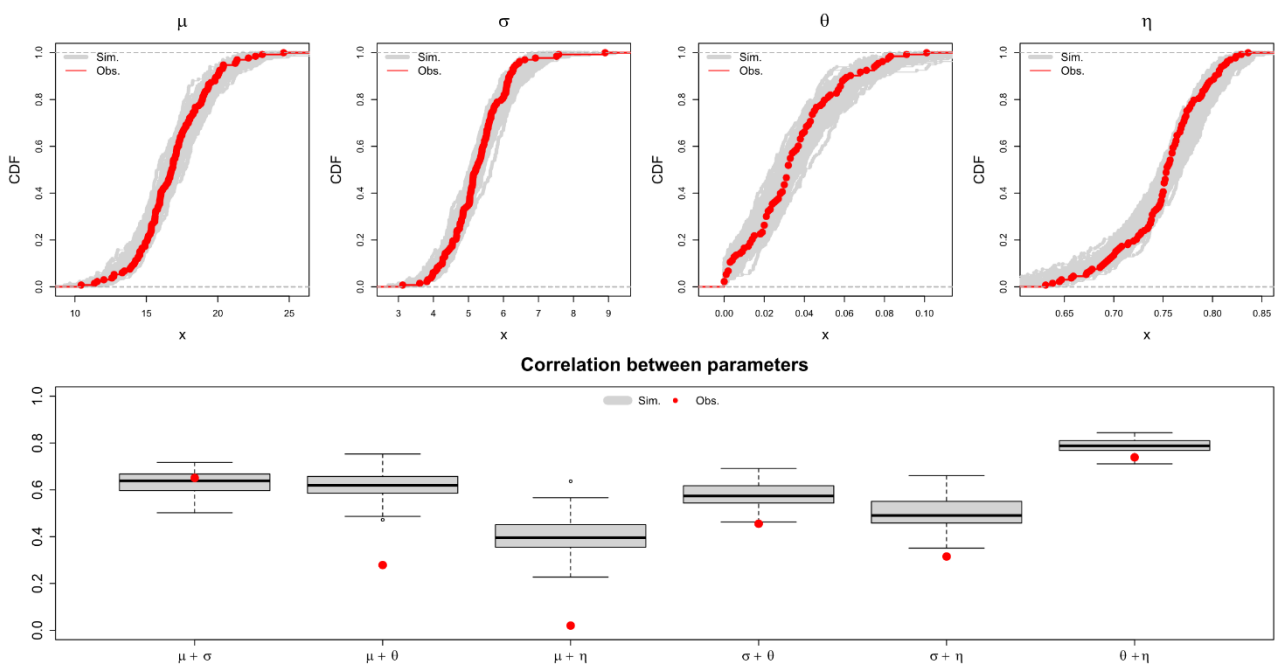


Figure 11 upper row - empirical CDF simulated from Exp.5 (in grey) and from observed parameter values (in red) over the 133 locations; lower row – observed correlations calculated in space between pairs of LS parameters (shown in red dots) and the respective correlations from 100 KED[LS|SS] simulations (shown in the grey boxplots).

559 In KOSTRA2010R, which provides design storms for Germany, no objective uncertainty analysis was performed to give
 560 the confidence intervals between 10-20% and hence should not be directly compared with the objective uncertainty esti-
 561 mation performed here. The total uncertainty considered here (from Exp. 5) depends not only on the return period, but as
 562 well on the duration level. The results from **Figure 10** can be used to determine the tolerance above (+) and below (-) the
 563 median for the 95% confidence level. This will result in a median uncertainty range from ± 15 -25% for low return periods

564 (lower than 10 years), and from ± 20 -40% for high return periods (higher than 10 years). Moreover, the short durations
 565 (5min to 2 hours) are in general 20-30% more uncertain than the longer durations (6hours – 1 day). The behaviour exhib-
 566 ited here is in accordance also with other studies (for instance Marra et al., 2017) where the shorter duration intervals are
 567 more uncertain than the ones of 1 day. In this section we compare the uncertainty estimation from two experiments 4 and
 568 5, to see how they distinguish from one another. Uncertainty from experiment 1 is left outside, not only to keep the
 569 graphics simple for visualization, but also because it is much narrower than for the other 2 experiments and it is enclosed
 570 in Exp. 5. Examples of Depth-Duration-Frequency Curves and tolerance ranges for three stations and three returns periods
 571 ($T=1, 10$ and 100 years) are illustrated in **Figure 12** for three methods: only spatial KED[LS|SS] simulations (from Exp.
 572 4) in blue, local and spatial simulations (from Exp. 5) in orange, and local derived DDF curves in dashed black line. Note
 573 that the results shown here are also obtained in cross-validation mode, which of course overestimate the overall uncer-
 574 tainty at these locations. The first station KO00830 is located in Oberstdorf (a town in the Allgäu Alps of Germany), the
 575 second KO00490 in Soltau Lower Saxony, and the third KO00550 in Emmendingen in the Black Forest region. These
 576 three stations were selected as representative of different regions and behaviours. Over all the stations, the tolerance range
 577 computed by the two experiments are wider at short duration intervals. This is true for all return periods, but the tolerance
 578 ranges get wider with increasing return period. As seen from– first row, the expected rainfall depth in the German Alps is

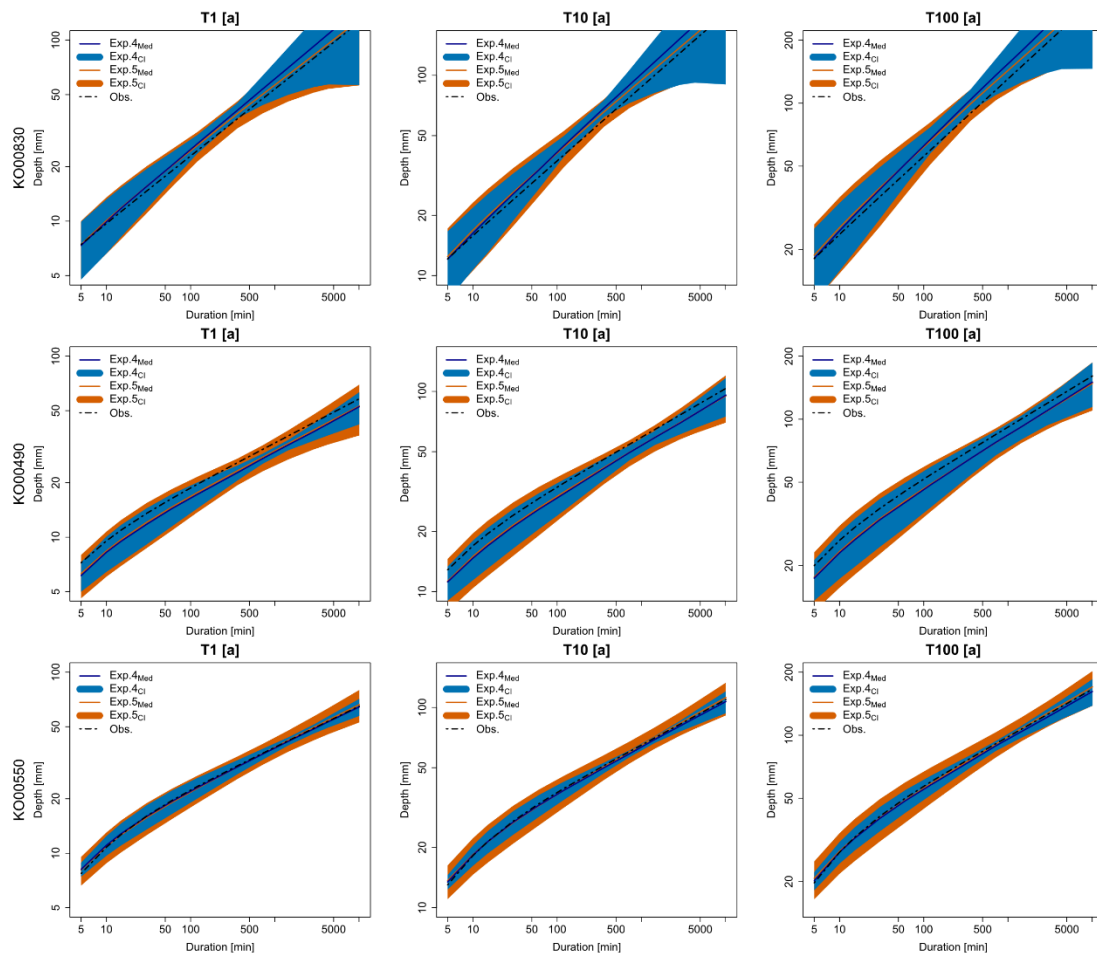


Figure 12 Examples of DDF estimates from observed data and predicted by simulations of Exp. 4 and 5 in a cross-validation mode: as median over all simulations and as 95% tolerance ranges from all simulations: upper row for return period $T=1$ years, middle row for $T=10$ years and lower row for return period $T=100$ years. Three stations are shown here: KO00830 located in the German-Alps, KO00490 location in Lower Saxony, and KO00550 located in Black Forest.

579 much higher than the two others, followed by the station in Soltau and the one in the Black Forest. Because of the low
580 station density in the Alp region, the tolerance range is bigger than in other locations. Overall the two products are similar
581 with each other, with the main difference present mainly at the durations from 6 to 12 hours, where Exp. 5 exhibits wider
582 tolerance ranges. Regarding the median estimation of DDF from both experiments, the main difference is seen in the Alps,
583 where the Exp. 5 agrees better with the observed values. Lastly, we recommend quantifying the uncertainty based on Exp.
584 5, since the tolerance ranges are better representing the duration levels from 6-12 hours and its median is matching better
585 with the observation.

586 **4.3 Spatial structure of uncertainty for whole Germany**

587 Spatial maps of precision were generated for three experiments (Exp. 1, 4 and 5), by using the whole dataset, in order to
588 investigate the spatial distribution of the precision when generating the DDFs curves for Germany. The precision in terms
589 of $nCI95_{width}$ [%] for the 4 parameters describing the extreme value statistics are given in **Figure 13**. It can be seen that
590 the different sources of uncertainties exhibit different precision over Germany. For instance, a propagation of the local
591 uncertainty (Exp. 1 showed at the first row), is causing less precision at observed locations (shown in black) than at
592 unobserved location. This is because, the resampling of the target network (LS) proves more uncertainty than resampling
593 the external drift network (SS). Therefore, uncertainty estimated from Exp. 1 is not enough to capture the spatial structure
594 of the uncertainties. On the other hand, Exp. 4 shows a clear spatial structure for uncertainty (mainly for three parameters
595 σ , θ , and η) with the North-West and South of Germany having higher uncertainty ranges. This follows the precipitation
596 regime and the station density in Germany; the South parts records higher precipitation amounts because of the German
597 Alps (so it is a region with clearly different behaviour than the rest of Germany), while the North-West has a lower station
598 density for both the LS and SS datasets in comparison with the rest of Germany. The uncertainty range at two parameters
599 μ and σ is increasing with 30-40% for whole Germany when combining the local with spatial uncertainty (Exp. 5) in
600 comparison with only spatial uncertainty (Exp. 4). The uncertainty at the parameters θ and η remains more or less at
601 similar levels, with similar spatial patterns. Thus, including the local uncertainty mainly influences the parameters of the
602 GEV distributions. It is interesting to see in Exp. 5, that at the location of the long recording stations (shown in black
603 squares), the uncertainty of the parameters μ and σ is much lower than for the rest of the regions. This is an expected
604 behaviour, as observed locations should be more certain than unobserved ones, and as the station density decreases, so
605 increases the uncertainty. This behaviour, not seen in other experiments, seems to be captured quite well by Exp. 5. This
606 is particularly true for the GEV parameters, while the Koutsoyiannis parameters show an additional spatial variability of
607 uncertainty that follows the main elevation features in Germany (represented by the external drift): with North-West and
608 South Germany having higher uncertainty ranges. Another interesting point is the high uncertainty associated at the σ
609 parameter by Exp. 5 at Münster city (shown in a red circle) which is as well visible at Exp. 1. The high uncertainty of the
610 scale parameters comes mainly from the local resampling bootstrap. As discuss in Shehu et. al (2022) a very rare extreme
611 event has been recorded in 2014 in Münster, which affects the extreme value analysis considerably. Thus, the integration
612 of the local uncertainty becomes mandatory to estimate the uncertainty when including these rare events (with a very high
613 return period) in the estimation of DDF curves for design purposes.

614 **Figure 14** illustrates the spatial distribution of uncertainty (computed here in term of precision $nCI95_{width}$ [%]) for the
615 durations 5min, 1hour, and 1 day and return period of 100 years: upper row - only from local uncertainty (Exp. 1), second
616 row – only from spatial uncertainty (Exp. 4) and lower row – from both local and spatial uncertainty (Exp. 5). The
617 uncertainty ranges exhibited by Exp. 1 (only considering the local uncertainty) are very similar throughout all three
618 durations and maintain similar spatial structure as with the parameter uncertainty in **Figure 13**. Here, the difference
619 between observed and unobserved locations is small and, following the parameter precision, the observed locations have
620 higher uncertainty than the unobserved ones (on average 15-20% higher $nCI95_{width}$ values). In Exp. 4 there is a clear

621 difference between the uncertainties of different durations, where the uncertainty of very short and very long durations
 622 (5min and 1 day) are governed by the spatial structure of θ and η parameters. The uncertainty of 1-hour durations are more
 623 or less uniformly distributed, but with the North-West region exhibiting higher uncertainties than the rest of Germany. At
 624 Exp. 5 the uncertainty for 5min durations has been increased considerably when including the local uncertainty (from 20-
 625 55% in Exp. 4 to 80-100%). The uncertainty of 1-hour durations exhibits similar patterns but is increased slightly from
 626 45% to 55% at Exp. 5. For 1-day duration, the uncertainty ranges are as well increased by Exp. 5, with values higher at
 627 the southern part of Germany (where the German Alps are located) and at the northern part of Germany near to the North
 628 Sea. The extreme event at Münster, influences the uncertainty of all durations but has a higher impact of short durations.
 629 Based on such propagation of uncertainty, tolerance ranges between $\pm 30-60\%$ should be expected in Germany for 5min
 630 duration intervals, $\pm 15-45\%$ for 1-hour durations and $\pm 20-50\%$ for 1-day durations. Overall, the combination of local

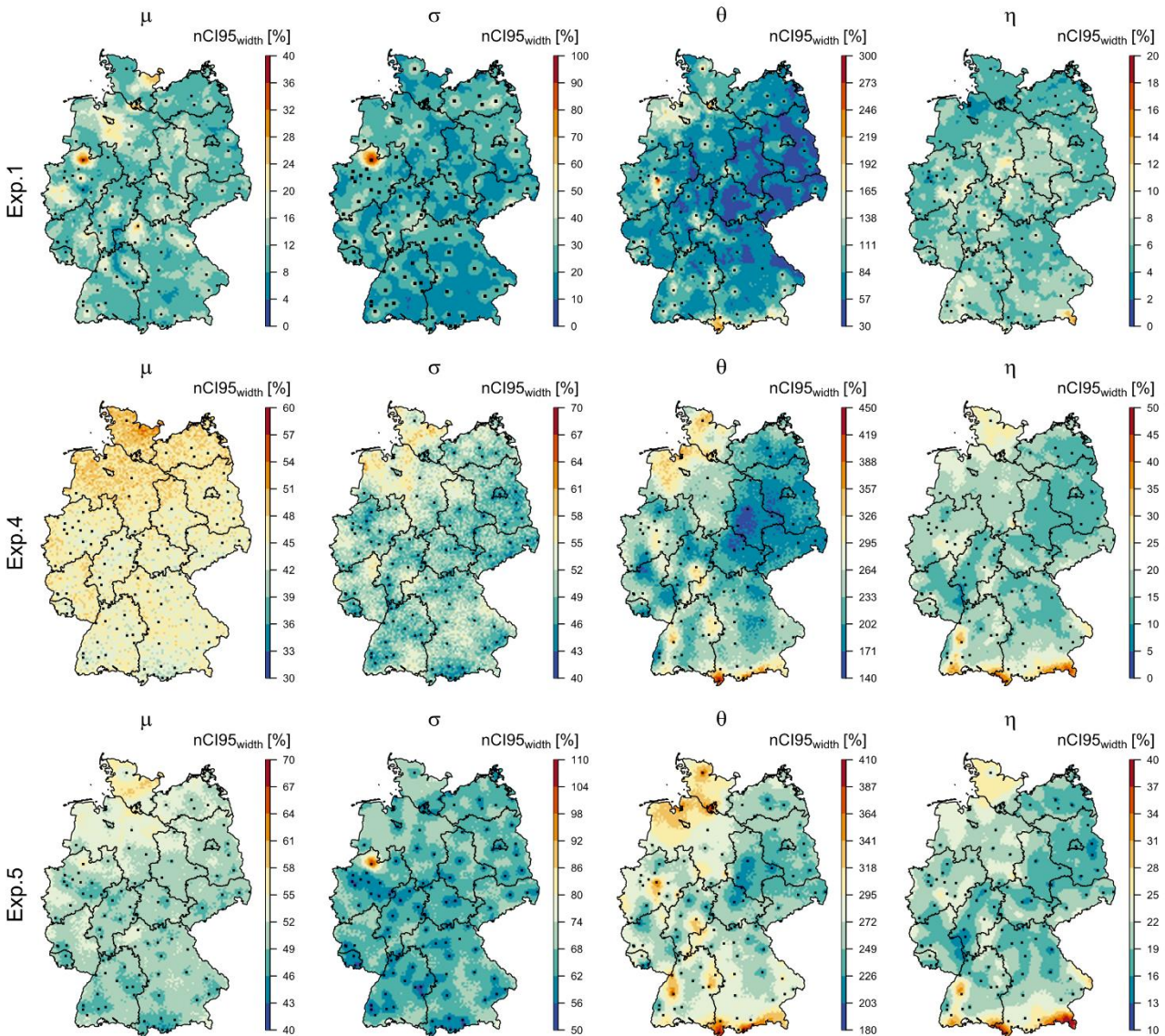


Figure 13 The precision ($nCI95[\%]$) in estimating the 4 parameters for the whole Germany with all available data for two experiments: upper row – results obtained from the propagation of 100 local resampled data to the final regionalisation (Exp. 1), middle row - results obtained from 100 spatial simulations of $KED[LS|SS]$ (Exp. 4), lower row – results obtained from 10,000 local resampling and spatial simulations of $KED[LS|SS]$ (Exp. 5). The black squares indicate the locations of LS, while the black lines illustrate the boundaries of German Federal states. Note that the ranges for the legend colours are changing for each experiment in order to emphasize the spatial structure of each experiment.

631 resampling with geostatistical spatial simulations provides the best method for the assessment of uncertainty in
 632 regionalisation DDF curves in Germany. First, and most importantly, the precision of these curves is higher at the location
 633 of long recording stations, and decreases in ungauged locations according to the distance from the long observations and
 634 the density of the observations in the vicinity.

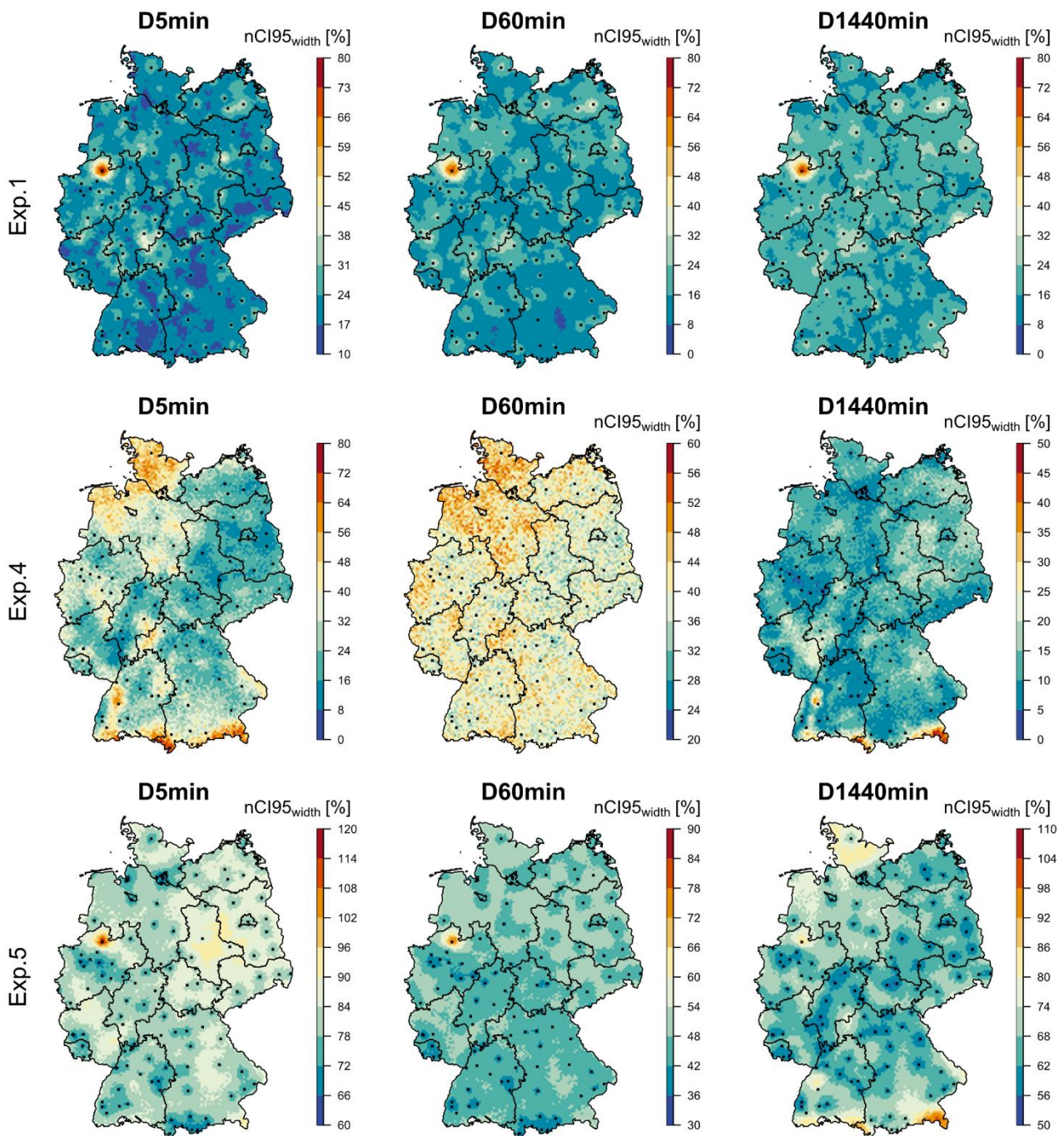


Figure 14 The precision ($nCI_{95}[\%]$) in estimation rainfall depth at different durations and 100 year return period for whole Germany with all available data for three experiments: upper row – results obtained from the propagation of 100 local resampled data to the final regionalisation (Exp. 1), middle row – results obtained from 100 spatial simulations of $KED[LS|SS]$ (Exp. 4), lower row – results obtained from 10,000 local resampling and spatial simulations of $KED[LS|SS]$ (Exp. 5). The black squares indicate the locations of LS, while the black lines illustrate the boundaries of German Federal states. Note that the ranges for the legend colours are changing for each experiment in order to emphasize the spatial structure of each experiment.

5. Conclusion and Outlook

635 In Shehu et al. (2022), a regionalisation based on external drift kriging was employed to calculate Depth-Duration-
636 Frequency (DDF) curves in Germany. Based on these results, an uncertainty analysis was conducted here to estimate the
637 precision of the obtained regionalised DDF curves in Germany. For this purpose, many simulations were performed at
638 the main components of the regionalisation procedure: local estimation of the extreme statistics (by non-parametric
639 bootstrapping), spatial dependency (by variogram bootstrapping) of short and long recording stations statistics, the
640 external drift information (by Sequential Gaussian Simulations) and the interpolation (also with Sequential Gaussian
641 Simulations). Four different experiments were run in order to estimate how the uncertainty at each component propagates
642 to the final regionalisation of the DDF curves, and a last experiment was performed by combing the uncertainty of the
643 two main components in order to assess the total uncertainty. The uncertainty, in terms of precision, was evaluated at each
644 long recording station location (on a cross-validation mode) based on the obtained 95% confidence interval from different
645 simulations. The conclusions from this investigation are summarised below:

- 647 • A comparison with Simulated Annealing showed that the SGS is better suitable for the study at hand, as it shows
648 higher accuracy by capturing better the inter-relationship between the parameters (despite of the data
649 transformation). Further works may include a new SA algorithm that models of the 4 parameters together in
650 space in order to keep the inter-relationship between them. A future improved SA algorithm may have the
651 potential to decrease the overall uncertainty ranges of DDF curves further on.
- 652 • The uncertainty from the variograms, that describes the spatial dependencies within the short and long
653 observation datasets, does not seem to influence much the final regionalisation of parameters and hence the
654 estimation of the DDF curves. Therefore, it was neglected for the total uncertainty propagation. On the other
655 hand, the uncertainty from the regionalisation of the long observations is the biggest source of uncertainty,
656 followed up by the local estimation of extremes and by the drift estimation from short observation. A
657 bootstrapping technique that combines the local estimation of extremes together with different spatial
658 simulations of the long observations, provided the highest uncertainty and was used to quantify the total
659 uncertainty.
- 660 • The total uncertainty obtained here follows mainly the behaviour of the spatial uncertainty, but is slightly higher,
661 as it is influenced by the local uncertainty. However, unlike the spatial uncertainty, the total uncertainty is
662 influenced by the very rare extreme events, and considers them as well for the computation of tolerance ranges.
663 Moreover, by combining local resampling with spatial simulations, the modelled uncertainty exhibits a valid
664 behaviour: at observed locations the precision is higher, and it decreases at unobserved locations according to
665 the distance from the observed, and the density of the observed locations in the vicinity. For very short and very
666 long durations, uncertainty ranges are also dependent on different climatological regions in Germany.
- 667 • From 10,000 simulation, it is concluded that the durations shorter than 2 hours exhibit a larger uncertainty that
668 longer durations, which of course is increasing with the return period considered. Depending on the location and
669 duration, tolerance ranges from $\pm 10\text{-}30\%$ for low return periods (lower than 10 years), and from $\pm 15\text{-}60\%$ for
670 high return periods (higher than 10 years) should be expected.
- 671 • For the proposed methodology, the uncertainty variation in space (for most locations) seems to be smaller ($\sim 10\text{-}$
672 20%) than the variation across different durations (up to 30%). On the other hand, the uncertainty variation due
673 to the return periods is low, approximately 5 to 10%. The only exception is at Münster, where a very rare extreme
674 events has been observed and causes high uncertainty ranges for the extreme values in the vicinity. Events such
675 at the one in Münster, influence the DDF curves considerably, and hence more research should be done in order
676 to investigate how to treat them when the focus is on DDF curves for return periods up to 100 years.

677 Overall, the combination of local resampling with geostatistical spatial simulations provides a very suitable method for
678 the assessment of uncertainty in regionalisation DDF curves. As shown here, considering only local resampling for the
679 sample variability will underestimate the total uncertainty especially at very short duration interval and high return periods.
680 Therefore, it becomes crucial to include as well spatial simulations for the computation of uncertainties. In this study, the
681 extreme value analysis based on GEV was investigated, nevertheless it would be interesting to see if a meta-statistical
682 approach, as proposed by Marra et al. (2019a), can result in narrower tolerance ranges while keeping a higher accuracy.
683 So far, only the sample and spatial variability were included for the estimation of the uncertainties. Future works may as
684 well include non-stationarity due to climate change, and the change of uncertainty patterns in the future.

685 **6. Data Availability**

686 The daily and the short sub-daily network are made publicly available by the German Weather Service (DWD) and can
687 be accessed at https://opendata.dwd.de/climate_environment/CDC/. All R-codes can be provided by the corresponding
688 authors upon request.

689 **7. Authors Contribution**

690 Supervision and funding for this research were acquired by UH, the study conception, design and methodology were
691 performed by both authors, while the software, data collection, derivation and interpretation of results were handled
692 mainly by BS. BS prepared the original draft, which was revised by UH.

693 **8. Competing Interest**

694 The authors declare that they have no conflict of interest.

695 **9. Funding**

696 This research was funded by the German Ministry of Agriculture and Environment Mecklenburg-Vorpommern and the
697 Federal State Funding Programme "Water, Soil and Waste".

698 **10. Acknowledgements**

699 The results presented in this study are part of the research project "Investigating Different Methods for Revising and
700 Updating the Heavy Rainfall Statistics in Germany (MUNSTAR)", funded by the German Ministry of Agriculture and
701 Environment Mecklenburg-Vorpommern and the Federal State Funding Programme "Water, Soil and Waste" who are
702 gratefully acknowledged. We are also thankful for the provision and right to use the data from the German National
703 Weather Service (Deutscher Wetterdienst DWD), more specific Thomas Deutschländer and Thomas Junghänel, and to
704 Winfried Willems from the Institute of Hydrology, Applied Water Resources and Geoinformatics (IAWG) for their
705 contribution in the local extreme value analysis.

706 **11. References**

- 707 Asquith, W. H.: Lmomco: L-moments, censored L-moments, trimmed L-moments, L-comoments, and many distributions., 2021.
708 Bárdossy, A. and Hörning, S.: Random Mixing: An Approach to Inverse Modeling for Groundwater Flow and Transport Problems,
709 *Transp. Porous Media*, 114(2), 241–259, doi:10.1007/s11242-015-0608-4, 2016.
710 Bastante, F. G., Ordóñez, C., Taboada, J. and Matías, J. M.: Comparison of indicator kriging, conditional indicator simulation and
711 multiple-point statistics used to model slate deposits, *Eng. Geol.*, 98(1–2), 50–59, doi:10.1016/j.enggeo.2008.01.006, 2008.
712 Bourennane, H., King, D., Couturier, A., Nicoullaud, B., Mary, B. and Richard, G.: Uncertainty assessment of soil water content spatial
713 patterns using geostatistical simulations: An empirical comparison of a simulation accounting for single attribute and a simulation
714 accounting for secondary information, *Ecol. Modell.*, 205, 323–335, 2007.
715 Burn, D. H.: A framework for regional estimation of intensity-duration-frequency (IDF) curves, *Hydrol. Process.*, 28(14),

716 doi:10.1002/hyp.10231, 2014.

717 Ceresetti, D., Ursu, E., Carreau, J., Anquetin, S., Creutin, J. D., Gardes, L., Girard, S. and Molinié, G.: Evaluation of classical spatial-
718 analysis schemes of extreme rainfall, *Nat. Hazards Earth Syst. Sci.*, 12(11), 3229–3240, doi:10.5194/nhess-12-3229-2012, 2012.

719 Chaudhuri, R. R. and Sharma, P.: Addressing uncertainty in extreme rainfall intensity for semi-arid urban regions: case study of Delhi,
720 India, *Nat. Hazards*, 104(3), doi:10.1007/s11069-020-04273-5, 2020.

721 Cinnirella, S., Buttafouco, G. and Pirrone, N.: Stochastic analysis to assess the spatial distribution of groundwater nitrate concentrations
722 in the Po catchment (Italy), *Environ. Pollut.*, 133, 569–580, 2005.

723 Coles, S.: *An Introduction to Statistical Modeling of Extreme.*, 2001.

724 CSöRgő, S. and Faraway, J. J.: The Exact and Asymptotic Distributions of Cramér-Von Mises Statistics, *J. R. Stat. Soc. Ser. B*, 58(1),
725 221–234, doi:10.1111/j.2517-6161.1996.tb02077.x, 1996.

726 Deutsch, C. V. and Journel, A. G.: *GSLIB: geostatistical software library and user's guide*. Second edition., 1998.

727 DVWK: *Statistische Analyse von Hochwasserabflüssen*, Merkblatt 251, Bonn, 62 S, 1999.

728 DWA: *Arbeitsblatt DWA-A 531: Starkregen in Abhängigkeit von Wiederkehrzeit und Dauer*, DWA Arbeitsgruppe HW 1.1e, Hennef,
729 Deutschland., 2012.

730 Emery, X.: Multi-gaussian kriging and simulation in the presence of an uncertain mean value, *Stoch. Environmental Res. Risk Assess.*,
731 24, 211–219, doi:10.1007/s00477-009-0311-5, 2010.

732 Ersoy, A. and Yünel, T. Y.: Assessment of lignite quality variables: A practical approach with sequential Gaussian simulation, *Energy*
733 *Sources, Part A Recover. Util. Environ. Eff.*, 31(2), 175–190, doi:10.1080/15567030701522260, 2009.

734 Fischer, S. and Schumann, A. H.: Berücksichtigung von Starkregen in der Niederschlagsstatistik, *Hydrol. und Wasserbewirtschaftung*,
735 62(4), 221–240, doi:10.5675/HyWa, 2018.

736 Forestieri, A., Lo Conti, F., Blenkinsop, S., Cannarozzo, M., Fowler, H. J. and Noto, L. V.: Regional frequency analysis of extreme
737 rainfall in Sicily (Italy), *Int. J. Climatol.*, 38(January), e698–e716, doi:10.1002/joc.5400, 2018.

738 Goovaerts, P.: Geostatistical tools for deriving block-averaged values of environmental attributes, *Geogr. Inf. Sci.*, 5(2), 88–96,
739 doi:10.1080/10824009909480518, 1999a.

740 Goovaerts, P.: Geostatistics in soil science: state-of-the-art and perspectives, *Geoderma*, 89, 1–45, 1999b.

741 Goovaerts, P.: Estimation or simulation of soil properties? An optimization problem with conflicting criteria, *Geoderma*, 97(3–4), 165–
742 186, doi:10.1016/S0016-7061(00)00037-9, 2000.

743 Goovaerts, P.: Geostatistical modelling of uncertainty in soil science, *Geoderma*, 103, 3–26, 2001.

744 Gyasi-Agyei, Y. and Pegram, G.: Interpolation of daily rainfall networks using simulated radar fields for realistic hydrological
745 modelling of spatial rain field ensembles, *J. Hydrol.*, 519(PA), 777–791, doi:10.1016/j.jhydrol.2014.08.006, 2014.

746 Haese, B., Hörning, S., Chwala, C., Bardossy, A., Schalge, B. and Kunstmann, H.: Stochastic reconstruction and interpolation of
747 precipitation fields using combined information of commercial microwave links and rain gauges, *Water Resour. Res.*, 53, 10,740–
748 10,756, 2017.

749 Hofmann, T., Darsow, A. and Schafmeister, M. T.: Importance of the nugget effect in variography on modeling zinc leaching from a
750 contaminated site using simulated annealing, *J. Hydrol.*, 389(1–2), 78–89, doi:10.1016/j.jhydrol.2010.05.024, 2010.

751 Hosking, J. R. M. and Wallis, J. R.: *Regional Frequency Analysis*, Cambridge University Press., 1997.

752 Jang, C. S.: Geostatistical analysis for spatially characterizing hydrochemical features of springs in Taiwan, *Environ. Earth Sci.*, 73(11),
753 7517–7531, doi:10.1007/s12665-014-3924-z, 2015.

754 Jang, C. S. and Huang, H. C.: Applying spatial analysis techniques to assess the suitability of multipurpose uses of spring water in the
755 Jiaosi Hot Spring Region, Taiwan, *Environ. Monit. Assess.*, 189(7), doi:10.1007/s10661-017-6029-9, 2017.

756 Journel, A. G. and Posa, D.: Characteristic behavior and order relations for indicator variograms, *Math. Geol.*, 22(8), 1011–1025, 1990.

757 Junghänel, T., Ertel, H. and Deutschländer, T.: *Bericht zur Revision der koordinierten Starkregenregionalisierung und -auswertung des*
758 *Deutsches Wetterdienstes in der Version 2010*, Tech. Rep., Offenbach am Main, Germany., 2017.

759 Junghänel, T., Bär, F., Deutschländer, T., Haberlandt, U., Otte, I., Shehu, B., Stockel, H., Stricker, K., Thiele, L.-B. and Willems, W.:
760 *Methodische Untersuchungen zur Novellierung der Starkregenstatistik für Deutschland (MUNSTAR)*, Synthesebericht., 2022.

761 Koutsoyiannis, D.: Statistics of extremes and estimation of extreme rainfall: I. Theoretical investigation, *Hydrol. Sci. J.*, 49(4), 575–
762 590, doi:10.1623/hysj.49.4.575.54430, 2004a.

763 Koutsoyiannis, D.: Statistics of extremes and estimation of extreme rainfall: II. Empirical investigation of long rainfall records, *Hydrol.*
764 *Sci. J.*, 49(4), 591–610, doi:10.1623/hysj.49.4.591.54424, 2004b.

765 Koutsoyiannis, D., Kozonis, D. and Manetas, A.: A mathematical framework for studying rainfall intensity-duration-frequency
766 relationships, *J. Hydrol.*, 206(1–2), 118–135, doi:10.1016/S0022-1694(98)00097-3, 1998a.

767 Koutsoyiannis, D., Kozonis, D. and Manetas, A.: intensity-duration-frequency relationships, *J. Hydrol.*, 206, 118–135, 1998b.

768 Liao, K., Lai, X., Lv, L. and Zhu, Q.: Uncertainty in predicting the spatial pattern of soil water temporal stability at the hillslope scale,
769 *Soil Res.*, 54(6), 739–748, doi:10.1071/SR15059, 2016.

770 Lin, Y.-P. and Chang, T.-K.: Simulated annealing and kriging method for identifying the spatial patterns and variability of soil heavy
771 metal, *J. Environ. Sci. Heal. Part A*, 35(7), 1089–115, 2000.

772 Luca, C., Si, B. C. and Farrell, R. E.: Assessing spatial distribution and joint uncertainty of TPH-fractions: Indicator kriging and
773 sequential indicator simulation, *Can. J. Soil Sci.*, 87(5), 551–563, doi:10.4141/CJSS07003, 2007.

774 Marra, F., Morin, E., Peleg, N., Mei, Y. and Anagnostou, E. N.: Intensity-duration-frequency curves from remote sensing rainfall
775 estimates: Comparing satellite and weather radar over the eastern Mediterranean, *Hydrol. Earth Syst. Sci.*, 21(5), 2389–2404,
776 doi:10.5194/hess-21-2389-2017, 2017.

777 Marra, F., Zoccatelli, D., Armon, M. and Morin, E.: A simplified MEV formulation to model extremes emerging from multiple
778 nonstationary underlying processes, *Adv. Water Resour.*, 127, doi:10.1016/j.advwatres.2019.04.002, 2019a.

779 Marra, F., Nikolopoulos, E. I., Anagnostou, E. N., Bárdossy, A. and Morin, E.: Precipitation frequency analysis from remotely sensed
780 datasets: A focused review, *J. Hydrol.*, 574(March), 699–705, doi:10.1016/j.jhydrol.2019.04.081, 2019b.

781 Miniussi, A. and Marra, F.: Estimation of extreme daily precipitation return levels at-site and in ungauged locations using the simplified
782 MEV approach, *J. Hydrol.*, 603(PB), 126946, doi:10.1016/j.jhydrol.2021.126946, 2021.

783 Namysłowska-Wilczyńska, B.: Application of turning bands technique to simulate values of copper ore deposit parameters in Rudna
784 mine (Lubin-Sieroszowice region in SW part of Poland), *Georisk*, 9(4), 224–241, doi:10.1080/17499518.2015.1104363, 2015.

785 NASA Shuttle Radar Topography Mission (SRTM)(2013). Shuttle Radar Topography Mission (SRTM) Global.
786 Distributed by OpenTopography. <https://doi.org/10.5069/G9445JDF>. Accessed: 2023-02-09

787 Notaro, V., Liuzzo, L., Freni, G. and Loggia, G. La: Uncertainty analysis in the evaluation of extreme rainfall trends and its implications
788 on urban drainage system design, *Water (Switzerland)*, 7(12), doi:10.3390/w7126667, 2015.

789 Overeem, A., Buishand, A. and Holleman, I.: Rainfall depth-duration-frequency curves and their uncertainties, *J. Hydrol.*, 348(1–2),
790 124–134, doi:10.1016/j.jhydrol.2007.09.044, 2008.

791 Overeem, A., Buishand, T. A. and Holleman, I.: Extreme rainfall analysis and estimation of depth-duration-frequency curves using
792 weather radar, *Water Resour. Res.*, 45, W10424, doi:10.1029/2009WR007869, 2009.

793 Pebesma, E. J.: Multivariable geostatistics in S: The gstat package, *Comput. Geosci.*, 30(7), 683–691, doi:10.1016/j.cageo.2004.03.012,
794 2004.

795 Pebesma, E. J. and Wesseling, C. G.: Gstat: A program for geostatistical modelling, prediction and simulation, *Comput. Geosci.*, 24(1),
796 17–31, doi:10.1016/S0098-3004(97)00082-4, 1998.

797 Perica, S., Pavlovic, S., St. Laurent, M., Trypaluk, C., Unruh, D., Martin, D. and Wilhite, O.: NOAA Atlas 14 Volume 10: Precipitation-
798 Frequency Atlas of the United States, NOAA, Natl. Weather Serv. Silver Spring, MD, 1, 2019.

799 Poggio, L., Gimona, A., Brown, I. and Castellazzi, M.: Soil available water capacity interpolation and spatial uncertainty modelling at
800 multiple geographical extents, *Geoderma*, 160(2), 175–188, doi:10.1016/j.geoderma.2010.09.015, 2010.

801 Poschlod, B.: Using high-resolution regional climate models to estimate return levels of daily extreme precipitation over Bavaria, *Nat.*
802 *Hazards Earth Syst. Sci.*, 21(11), 3573–3598, doi:10.5194/nhess-21-3573-2021, 2021.

803 Requena, A. I., Burn, D. H. and Coulibaly, P.: Pooled frequency analysis for intensity–duration–frequency curve estimation, *Hydrol.*
804 *Process.*, 33(15), doi:10.1002/hyp.13456, 2019.

805 Ribeiro, M. C. and Pereira, M. J.: Modelling local uncertainty in relations between birth weight and air quality within an urban area:
806 combining geographically weighted regression with geostatistical simulation, *Environ. Sci. Pollut. Res.*, 25(26), 25942–25954,
807 doi:10.1007/s11356-018-2614-x, 2018.

808 Shehu, B., Willems, W., Stockel, H., Thiele, L.-B. and Haberlandt, U.: Regionalisation of Rainfall Depth-Duration-Frequency curves

809 in Germany, *Hydrol. Earth Syst. Sci.*, [preprint], 2022.

810 Szatmári, G. and Pásztor, L.: Comparison of various uncertainty modelling approaches based on geostatistics and machine learning
811 algorithms, *Geoderma*, 337(September 2018), 1329–1340, doi:10.1016/j.geoderma.2018.09.008, 2019.

812 Tfwala, C. M., van Rensburg, L. D., Schall, R., Mosia, S. M. and Dlamini, P.: Precipitation intensity-duration-frequency curves and
813 their uncertainties for Ghaap plateau, *Clim. Risk Manag.*, 16, doi:10.1016/j.crm.2017.04.004, 2017.

814 Uboldi, F., Sulis, A. N., Lussana, C., Cislighi, M. and Russo, M.: A spatial bootstrap technique for parameter estimation of rainfall
815 annual maxima distribution, *Hydrol. Earth Syst. Sci.*, 18(3), 981–995, doi:10.5194/hess-18-981-2014, 2014.

816 Varouchakis, E. A.: Median polish kriging and sequential gaussian simulation for the spatial analysis of source rock data, *J. Mar. Sci.*
817 *Eng.*, 9(7), doi:10.3390/jmse9070717, 2021.

818 Van de Vyver, H.: Bayesian estimation of rainfall intensity-duration-frequency relationships, *J. Hydrol.*, 529,
819 doi:10.1016/j.jhydrol.2015.08.036, 2015.

820 Watkins, D. W., Link, G. A. and Johnson, D.: Mapping regional precipitation intensity duration frequency estimates, *J. Am. Water*
821 *Resour. Assoc.*, 41(1), doi:10.1111/j.1752-1688.2005.tb03725.x, 2005.

822 Yang, Y., Tian, Q., Yang, K., Meng, C. and Luo, Y.: Using Sequential Gaussian Simulation to Assess the Spatial Uncertainty of PM 2.5
823 in China, *Int. Conf. Geoinformatics*, 2018-June(41761084), 1–5, doi:10.1109/GEOINFORMATICS.2018.8557167, 2018.

824